Aerospace Science and Technology 115 (2021) 106774

Contents lists available at ScienceDirect

Aerospace Science and Technology

www.elsevier.com/locate/aescte

Experimental study of a helicopter model in shipboard operations

Neda Taymourtash [a,b,*], Daniele Zagaglia [b], Alex Zanotti [a], Vincenzo Muscarello [a], Giuseppe Gibertini [a], Giuseppe Quaranta [a]

[a] Department of Aerospace Science and Technology, Politecnico di Milano, Milan, Italy
[b] Aerospace Sciences Division, James Watt School of Engineering, University of Glasgow, Glasgow, UK

ARTICLE INFO

Article history:
Received 12 March 2020
Received in revised form 14 January 2021
Accepted 26 April 2021
Available online 3 May 2021
Communicated by Vassilis Theofilis

Keywords:
Helicopter
Wind tunnel experiment
Ship airwake
Aerodynamics
Multibody simulation

ABSTRACT

The paper presents the experimental investigation of the aerodynamic interaction between a helicopter model and a ship model with a simplified geometry. In the first phase of the experiment, a series of wind tunnel tests were carried out in order to study the flow features on the flight deck for several wind conditions, without the presence of the helicopter. Pressure measurements and Particle Image Velocimetry surveys were performed to assess the effect of wind velocity and direction on the flow field in the landing region over the ship deck. Moreover, the effect of the Atmospheric Boundary Layer was investigated. In the second phase of the experimental campaign, a helicopter model was positioned in a series of points representative of a typical stern landing trajectory and a vertical descent above the landing spot. The landing maneuver was performed in three different wind conditions, including no-wind, head wind and wind blowing from port side of the deck. The rotor loads and moments were measured by means of a six-axis balance for all test points. The use of different measurement techniques in the present experiments provides a comprehensive database suitable for the study of the rotor-ship aerodynamic interaction. Additionally, the experimental results are used to develop an identification algorithm to be incorporated into the flight simulator environment to capture the effect of ship airwake on the rotor loads during shipboard operations.

1. Introduction

Helicopters are regularly required to perform challenging missions in confined areas and close to obstacles. Search and rescue missions over land and water, urban transport, intervention in natural disasters, such as flooding, or earthquake, are some examples in which helicopters interact with the surrounding environment. In these situations, performance and handling qualities of the helicopter are highly affected by the presence of the obstacles in close proximity. The aerodynamic interaction could be even more complicated when the environment is non-stationary. A well-known example is offshore operations which are among the most demanding tasks for pilots. In this case, due to the combination of moving flight deck, flying close to the ship hangar wall, changing speed and direction of the wind and turbulent ship airwake, the pilot's workload is significantly increased which may endanger flight safety. It has been shown that the most of the frequency content of the unsteady airwake is concentrated in the range of 0.2-2 Hz [1]. This bandwidth covers the widely accepted range of pilot closed-loop control frequencies, characterized by a cross-over frequency lower than 1.6 Hz [2].

Safety analysis for such demanding missions needs a series of at-sea trials which are inherently hazardous and extremely expensive. Furthermore, each combination of ship-helicopter should be tested for a range of wind speed and direction in order to find the Ship-Helicopter Operational Limitations (SHOL) [3]. Consequently, development of the helicopter-ship Dynamic Interface (DI) simulation is considered as a viable solution which reduces the cost and hazards of time-consuming at-sea test campaigns [4]. Such a simulation tool could be used to find the optimal trajectory for safe landing and to design and test of new flight control systems. A better understanding of the environmental conditions could lead to the development of high-fidelity simulation environment to improve pilot training. All those elements will contribute to the improvement of safety of rotorcraft operations, which is the objective of the NITROS project [5].

Regarding the complexity of the flow field generated by the helicopter-ship interaction, development of an appropriate airwake model which can capture the induced airloads of the rotor is of

* Corresponding author at: Department of Aerospace Science and Technology, Politecnico di Milano, Milan, Italy.
E-mail addresses: Neda.Taymourtash@polimi.it (N. Taymourtash), Daniele.Zagaglia@glasgow.ac.uk (D. Zagaglia), Alex.Zanotti@polimi.it (A. Zanotti), Vincenzo.Muscarello@polimi.it (V. Muscarello), Giuseppe.Gibertini@polimi.it (G. Gibertini), Giuseppe.Quaranta@polimi.it (G. Quaranta).

https://doi.org/10.1016/j.ast.2021.106774

Nomenclature

A	Rotor disc area ..... m^2	Δv	Modification of the freestream velocity above the rotor disk ..... m/s
c	Blade chord ..... m	(X, Y, Z)	Absolute reference system
c_P	Pressure coefficient, $2(P - P_\infty)/(\rho U_\infty^2)$	(x, y, z)	Rotor reference system
c_T	Thrust coefficient, $T/\left(\rho\Omega^2 R^2 A\right)$	Z_{ref}	Height of the reference Pitot probe ..... mm
c_m	Pitch moment coefficient, $M/\left(\rho\Omega^2 R^2 AR\right)$	μ	Advance ratio, $U_\infty/(\Omega R)$
c_l	Roll moment coefficient, $L/\left(\rho\Omega^2 R^2 AR\right)$	$\lambda_0, \lambda_s, \lambda_c$	Inflow variables
H_w	Height of the ship hangar wall ..... mm	χ	Skew angle of the wake
L_d	Length of the ship deck ..... mm	ψ	Azimuth angle
L_{dr}	Length of the downstream recirculation zone mm	v_i	Induced velocity ..... m/s
L_s	Length of the ship superstructure ..... mm	ABL	Atmospheric Boundary Layer
r	Local radius of a rotor blade section ..... m	DI	Dynamic Interface
R	Rotor disc radius ..... m	GVPM	Galleria del Vento Politecnico di Milano
$\|\mathbf{U}\|$	In-plane velocity magnitude ..... m/s	IGE	In Ground Effect condition
U_∞	Free-stream wind velocity magnitude ..... m/s	OGE	Out of Ground Effect condition
(u, v, w)	Velocity components in rotor reference frame m/s	PIV	Particle Image Velocimetry
(u', v', w')	Root mean square of the velocity components m/s	RMS	Root Mean Square
v_{sh}	Flow distortion velocity ..... m/s	SF	Smooth Flow
		SHOL	Ship Helicopter Operational Limitations

great importance. Various numerical or experimental approaches can be taken for airwake modelling which result in different levels of simulation fidelity. In both numerical and experimental analysis of the shipboard operation, the effect of ship airwake and rotor wake coupling is worth considering. The most simplified approach is uncoupled simulation which means there is no interaction between rotorcraft and ship airwake. One-way coupling approach, which has been extensively implemented in flight simulation environments so far, accounts only for the effect of ship airwake on the rotor inflow. In this approach, the airwake of the ship is pre-calculated, using either steady or unsteady Computational Fluid Dynamics (CFD) without considering the presence of the helicopter. This method represents one of the few viable ways to perform pilot-in-the-loop real-time simulations. The ship airwake velocities are incorporated into the flight dynamics code via look-up tables, assuming superposition of the ship airwake and rotor induced flow. Based on subjective pilot workload ratings, this approach could reasonably capture the increased workload due to influence of the ship airwake, including the effect of unsteadiness [1,6]. However, the superposition method, has shown a low accuracy for cases of close proximity between the helicopter and structure of the ship. To assess the coupling effects on the helicopter flight characteristics, Crozon et al. [7] studied the ship-helicopter aerodynamic interaction simulating four different cases: isolated ship, isolated rotor, shipborne rotor and superposition of isolated rotor and ship. Both steady-state Reynolds-Averaged Navier-Stokes (RANS) with actuator disk method, and unsteady RANS using blade-resolving representation of the rotor were investigated. The results showed significant differences in rotor loading between isolated rotor in forward flight and near-deck operations which highlight the importance of coupling effects. The validity of this conclusion has been further investigated to determine the minimum distance between helicopter and a ground obstacle where the interaction can be considered negligible [8], that was quantified in an approximate distance of 5 main rotor radii away from the obstacle, independently of wind speed.

Consequently, for the interactive aerodynamic environment in shipboard operations, the most representative approach must be considered the two-way coupling, or fully-coupled simulation which includes mutual interaction of the helicopter and ship airwake. In this approach, the aerodynamic solver and flight dynamics simulation of the helicopter should be run simultaneously with communication between two codes. The flight dynamics code calculates the loading of the rotor, as well as the attitude and position of the helicopter, which are passed to the aerodynamic solver. Then, the local velocity data is computed by aerodynamic solver and fed back to the flight dynamics simulation [9–11]. Depending on the computational cost of the numerical algorithm to capture the aerodynamic interaction, this approach might be used in real time flight simulation. Towards this aim, Zhao et al. [12] developed a real-time rotor wake model by implementing the results of a rotorcraft/ship hybrid solver, which couples a viscous Vortex Particle Method (VPM) with an unstructured CFD solver, to augment the widely used Peters-He finite state dynamic wake model. In another effort to support real-time piloted simulation, a free-vortex wake model was developed and integrated with a US Navy flight dynamics simulation [13]. This model includes a vortex-based solution strategy to account for interactions between the rotor wake and an external spatial and time-varying disturbance field. The results of the coupled free wake aerodynamic and flight dynamics model were compared with flight test data for vertical descent and shipboard operations. VPM may represent a good compromise between accuracy and computational cost, however full RANS offer the most complete approach for a fully coupled simulation. In [14], Oruc et al. presented the recent advancements of an ongoing project towards this aim. They achieved the real-time execution of a DI simulation, with a fully-coupled Navier-Stokes CFD solver and a helicopter flight dynamic code (GENHEL-PSU) for the case of a simplified shedding wake. However, the final goal requires more substantial computing improvements, as indicated in [14].

A complementary approach to numerical simulation could be followed trying to understand and quantify the effects of the coupled ship helicopter wakes through scaled experiments performed in the wind tunnel. This approach has the additional advantage of providing a database of tests that could be exploited to better validate numerical simulation. As a matter of fact, the approach taken in this work relies on wind tunnel experiments to improve the capability of estimating the flow-field and consequently fidelity of flight simulation. This is the first step towards development of a fully-coupled flight dynamics simulation with wind tunnel in the loop, were the measures on a wind tunnel model could be coupled to a flight mechanics numerical model of the helicopter to simulate the approach trajectory and estimate potential problems that

may preclude the possibility to perform such a maneuver in a real flight, as it is usually done in DI tests.

One of the first experimental investigations in this field was done by Zan at Aerodynamic Laboratory, National Research Council of Canada, and is presented in [15–17]. The experiments were conducted at a geometric scale of 1:50 of the Canadian Patrol Frigate and CH-124 Sea King. An initial experiment focused on the measurements of the time averaged rotor thrust coefficients for the rotor immersed in Canadian Patrol Frigate airwake [15]. This study has demonstrated that the reduced inflow to the rotor, due to ship airwake, can significantly decrease rotor thrust up to 15%. The results also confirmed the strong influence of wind speed and direction on the airwake, and consequently on the rotor thrust and operational envelope of the helicopter. Another experiment was conducted using the same ship model, to measure unsteady loads acting on the rotor-less helicopter fuselage [16]. A reasonable correlation was found between Root Mean Square (RMS) loading levels and pilot workload obtained from flight test [16]. The additional influence of the rotor downwash on the unsteady loading of the fuselage was also studied and compared with rotor-less case [17].

Kääriä et al. proposed a different test setup to characterize the aerodynamic loading of a 1:54 model-scale helicopter immersed in the airwake of a generic frigate ship [18]. The experiments were conducted in a water tunnel using a specially designed Airwake Dynamometer (AirDyn) identifying specific time-averaged and unsteady loading characteristics caused by the severe spatial and temporal velocity gradients in the airwake. The setup has been used also to investigate the potential benefits of aerodynamic modifications to the ship geometry [19]. Various modifications were proposed and many were found effective in reducing the RMS of forces and moments. In particular, the promising design concepts were a side-flap and notch modification which both showed consistent improvements of 25-50% in loads RMS.

To identify the rotor downwash and ship airwake coupling, flow visualization techniques have been utilized as well which provide information on development of the interacting flowfield during the landing maneuver. Landman conducted an experiment, exploiting Particle Image Velocimetry (PIV) with the ship and rotor in isolation and then the combined case to investigate the superimposed velocity field and recirculation region [20,21]. Furthermore, an extensive rotor thrust survey was conducted highlighting significant variations close to the landing deck.

In addition to shipboard operations, there are some studies regarding the interaction of rotorcraft with simple shape obstacles, like buildings. For instance, Quinliven and Long evaluated the effects of the aerodynamic wake from a large upstream object, such as a building, on a rotorcraft operating in proximity to that object [22]. In this experiment, smoke visualization was used with high intensity light in order to visualize the flow field and, induced velocities were measured using the pressure probes distributed spanwise along each blade. The results showed that the presence of the upwind building tended to decrease the induced velocities at the leading edge of the rotor disc, which is consistent with the recirculation region between the rotor and building. A series of experiments were carried out at Politecnico di Milano by Zagaglia et al. to study helicopter interactions with a ground obstacle. Initial tests were aimed to replicate different hovering conditions in absence of wind [23]. Then, the performance of the rotor in moderate windy conditions was assessed for several positions with respect to the obstacle [24]. In particular, the helicopter model, including a four-bladed rotor and fuselage, was positioned in different points relative to a simplified volume with a box shape. The forces and moments acting on the rotor were measured with a six component strain gauge balance nested inside the fuselage. PIV survey was used to investigate the details of the interacting flow field. The results showed a strong modification of mean thrust and in-plane hub moments when the helicopter entered in the obstacle wake.

The present research work is aimed to provide a comprehensive experimental database suitable for the investigation of the interacting aerodynamic environment between helicopter and ship while approaching the flight deck. The experimental results presented can contribute to improve the fidelity of the simulation of such demanding flight phase by introducing the measured effects of the interacting flowfield. To this aim, two test campaigns were performed at large test chamber of the large Wind Tunnel of Politecnico di Milano (GVPM). Thanks to the dimensions of the wind tunnel test section a larger geometric scale with respect to the literature was used in the present experimental investigation for both the helicopter and ship models. The first campaign focused on a ship airwake characterization study without the presence of the helicopter. With this aim PIV surveys on longitudinal planes and pressure measurements were performed in the ship deck region. This campaign was devoted to assess the influence of the wind velocity, direction and Atmospheric Boundary Layer (ABL) on topology of the flow-field over the deck, and also to have a characterization of the baseline flowfield to be used to identify the effect of the ship-helicopter wake interaction in the following test campaigns. Then, a second campaign was carried out to simulate a typical landing trajectory and analyse the rotor loads in different positions with respect to the deck. During this campaign, the rotor forces and moments were measured by a six-components strain gauge balance, the rotor inflow was surveyed by PIV and pressure field was measured on both the flight deck and the hangar of the ship. The results presented will show the effect of the ship airwake on the mean rotor loads. Other effects were identified in the frequency spectrum of loads, however, due to limitation in the testing hardware used – in particular in the helicopter motor thermal management – the frequency resolution obtained was too low to provide reliable data for the range of interest. Consequently, the analysis of the effects of unsteadiness, and the consequent increase of pilot workload, has been postponed to future test campaigns.

Then, the experimental results were used to develop an identification algorithm aimed to reconstruct the average and linear variation of the inflow above the rotor disk by adding an airwake model representative of the interactions of the rotor with the ship airwake in the surrounding environment. This instrument can be considered an effective tool to obtain a more realistic representation of the shipboard operations in the simulation environment.

2. Experimental setup

The tests were carried out in the large test chamber of the GVPM which is 13.84 m wide, 3.84 m high and 35 m long. The test rig, as shown in Fig. 1, consists of a 4-bladed helicopter and a simplified ship model [25]. The helicopter model was held by a horizontal strut fixed to a system of two motorised orthogonal sliding guides which was able to change the relative position of the helicopter with respect to the ship in both vertical and longitudinal directions. A fixed coordinate system was defined to introduce the test points, which represents the position of the rotor hub center with respect to the ship. The $X-Z$ plane of this reference frame was aligned with the longitudinal symmetry plane of the flight deck, with the origin on the floor of the wind tunnel and the end of the stern, see Fig. 2(a).

2.1. Ship model

The ship model is a 1:12.5-scale model of Simple Frigate Shape 1 which is a highly simplified but representative ship geometry, developed as a part of an international collaboration in which Canada, Australia, New Zealand, UK and USA evaluated the ability

Fig. 1. The test rig mounted inside the GVPM large test chamber.

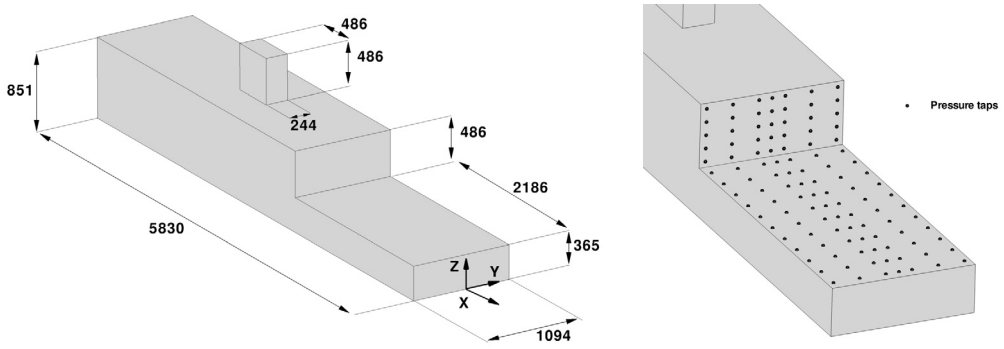

(a) Dimensions (in mm) (b) Pressure taps

Fig. 2. Sketch of the 1:12.5-scale model of SFS1 equipped with pressure taps.

of CFD codes to simulate complex airwakes [26]. The wind tunnel dimensions enabled selection of a geometric scale of 12.5, quite larger than models used in similar works in the literature [15,18]. This allowed for an experiment Reynolds number much closer to full scale values. The fore part of the ship was not reproduced, as the effect of this part on the airwake in the landing region was considered negligible. This choice allowed mounting of both the models and the traversing system on the large turn-table of the test section (13 m of diameter), and this in turn allowed easy investigation of the effect of wind direction. The ship model consists of a rectangular prism with a step on its rear and another prism on top which is acting like a ship superstructure, as represented in Fig. 2(a), reporting the main dimensions of the model. The landing point of the helicopter model was placed on the center of the turn-table, thus the ship can be rotated to both sides, while the landing point remains fixed with respect to the boundaries of the test section. The flight deck and hangar wall were equipped with 77 and 35 pressure taps respectively. The pressure measurements were performed using four low-range 32-ports pressure scanners embedded inside the ship model. The declared accuracy of the pressure scanners led to an estimated uncertainty for the pressure coefficient of approximately 0.15.

2.2. Helicopter model

The helicopter model was the same used for the investigation of the rotor-building aerodynamic interaction described in Refs. [23,24]. The model consisted of a fuselage and a rotor which has four untwisted and untapered rectangular blades, with NACA0012 airfoil, a chord of $c = 0.032$ m, and radius of $R = 0.375$ m. A rigid hub without hinges was adopted throughout this test campaign and the blades were rigidly connected to the hub with a very stiff connector and a constant pitch angle of 10°. Since the swashplate was not included, the rotor could not be trimmed to a target set of forces and moments. However, thanks to the rigid hub along with relatively stiff blades, the aeroelastic deformations were negligible. Consequently, the variation of loads while approaching the deck were expected to be dominated by the interactions with the obstacle and the flowfield generated by it, and so could be taken as an index to highlight and quantify the mean effects of the interactions on the rotor aerodynamics.

The rotor rotational speed of 2580 RPM was maintained in all tests by means of a brushless, low-voltage, electrical motor with an electric controller. A Hall-effect sensor giving the one per revolution signal was used as feedback signal for RPM control. The rotor rotational speed drift (less than 20 RPM) was considered in the evaluation of the force/moment coefficients as the rotor RPM were measured simultaneously with the force and moments during the test runs. The loads acting on the rotor were measured using a six-components strain gauge balance nested inside the fuselage. The nominal accuracy of the load measurements was 0.25% of the load cell full range on each axis, which results in approximately 0.4% and 0.48% of the Out-of-Ground Effect (OGE) thrust and torque values, respectively. In order to reduce the balance thermal drifts, each test point corresponded to a single run where the motor was started from rest and then stopped again at the end of the acquisition. The balance signals acquisition took place over a period of 5 seconds. Each test point measurement was repeated for three

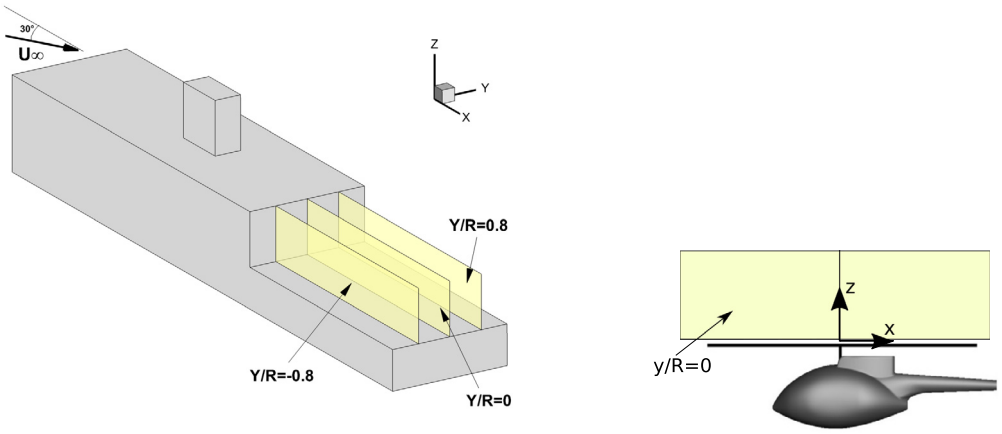

(a) Ship deck (b) Rotor inflow

Fig. 3. Position of the PIV investigation planes.

different runs and the results were averaged. A repeatability test over 30 measurements in the OGE condition ($Z/R = 4$) exhibited a standard deviation of the measured thrust and torque coefficients of about 0.3% [24].

2.3. PIV setup

The PIV system comprised a Litron NANO-L-200-15 Nd:Yag double-pulse laser with an output energy of 200 mJ and wavelength of 532 nm, and two Imperx ICL-B1921M CCD cameras with a 12-bit, 1952 × 1112 pixel array in tandem configuration. Each camera was equipped with a NIKKOR 50-mm lens. The laser was positioned on a suitable strut downstream of the ship model, so that the laser sheet was aligned with the X–Z plane. The laser was mounted on a longitudinal traversing system in order to cover the whole area of investigation along the shipdeck providing the same light power. The cameras line of sight was aligned perpendicular to the laser sheet.

The area of investigation of the first test campaign covered the whole shipdeck (more than 2 m × 0.5 m), thus, in order to achieve a better resolution of the image pairs, the measurement area included 10 multiple adjacent windows of 480 mm × 270 mm with a small overlapping among them. In the second campaign, two adjacent windows with the same dimensions of the previous tests, and with a small overlapping among them were surveyed to cover the longitudinal plane of the whole rotor disk for inflow investigation. In particular, the fore region of the disk was prioritised in the surveys in order to obtain more information on the rotor inflow. To avoid laser reflection over the blades during those tests, the closest line of the PIV area of investigation to the rotor was 48 mm above the disk plane. The data measured over this line were considered to extract the normal velocity along the longitudinal symmetry axis of the rotor. The position of the PIV measurement area for the two test campaigns is shown in Fig. 3.

The synchronisation of the two laser pulses with the image pair exposure was controlled by a six-channel Quantum Composer QC9618 pulse generator. A PIVpart30 particle generator by PIVTEC with Laskin atomizer nozzles was used for the seeding, which consisted of small oil droplets with diameters of 1-2 µm. The entire test section was filled with seeding during PIV tests. The image pair analysis was carried out using PIVview 2C software [27]. A single-pass interrogation was used for the correlation of the image pairs with an interrogation window of 64 × 64 pixels with an overlap factor of 50%. This led to a resolution of 8 mm between two adjacent measurement points. The results that will be shown in the following sections are the ensemble-average of the measurements over 800 image pairs acquired for each window. For those images the outlier regions are masked with a blank box.

The accuracy of the PIV measurement can be estimated considering a maximum displacement error of 0.1 px when using sub-pixel interpolation, as found in [28]. Taking into account the optical magnification and the pulse-separation time, which varied between 300 and 600 µs according to the local maximum velocity, the maximum in-plane velocity error is estimated to be between 0.04 and 0.08 m/s.

2.4. Atmospheric boundary layer

The GVPM Large test chamber is equipped with several devices allowing the production of different velocity profiles with different turbulence intensities. For the purpose of this study, two different free stream velocity profiles were considered. The Smooth Flow (SF), in which there were no upstream turbulators and so a uniform free stream velocity profile was generated, and the Atmospheric Boundary Layer (ABL), where turbulators were inserted upstream of the ship to obtain a velocity profile corresponding to the well-known power law model:

$$\frac{U}{U_{\text{ref}}} = \left(\frac{Z}{Z_{\text{ref}}}\right)^{\alpha} \tag{1}$$

where U is the mean velocity at height Z, U_{ref} is the reference velocity measured at height Z_{ref} and α is an exponent that depends on the roughness of the terrain. The ABL velocity profile generated in this experiment corresponds to the wind profile with $\alpha = 0.1$ which is suggested by Simiu et al. [29] for coastal areas. The wind tunnel free stream velocity for each test run was set using a Pitot probe placed above the ship superstructure. This choice was driven by the fact that anemometers are usually placed on ship's mast to be less affected by the ship airwake. In this experiment, the probe was positioned 180 mm above and 90 mm upstream of the top superstructure, as shown in Fig. 4. For the tests with red-wind, i.e. wind coming from the port side of the ship, the Pitot probe was adjusted in order to have the static port in the same position of the head-wind test.

Fig. 4 shows two adopted boundary layer profiles with respect to the ship size. Comparison of the ABL with the profile calculated by power law model shows a good agreement up to the reference height. Also, the profile of longitudinal turbulence intensity

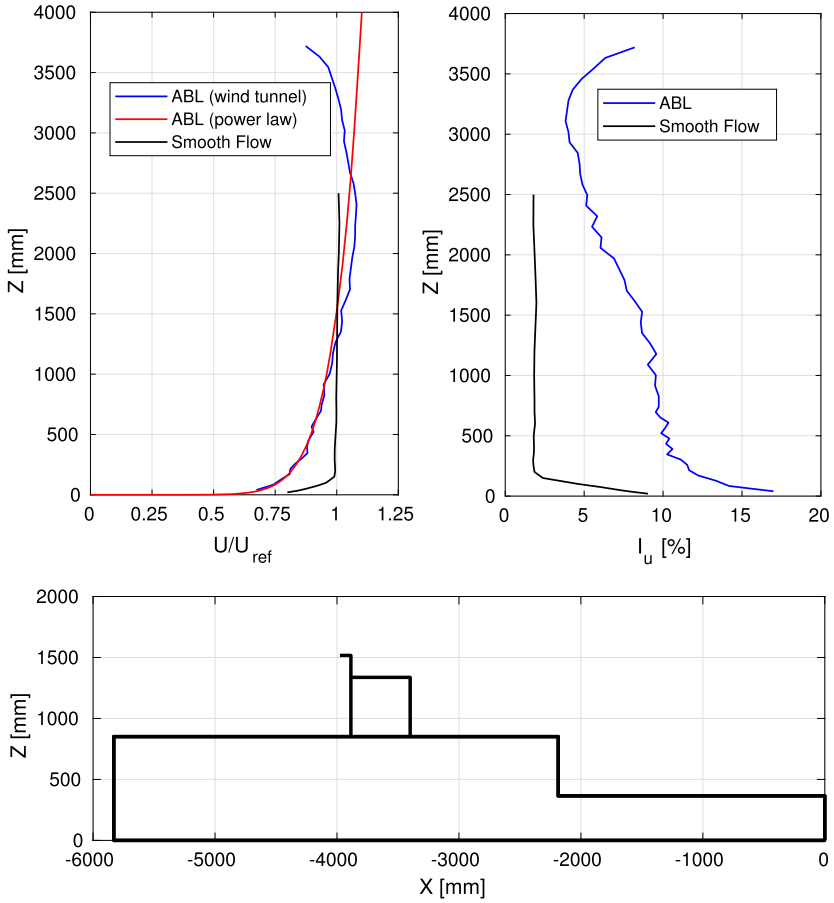

Fig. 4. Comparison of the mean velocity profile (top left) and turbulence intensity (top right) for ABL and SF. Ship dimensions (bottom) for reference. (For interpretation of the colours in the figure(s), the reader is referred to the web version of this article.)

shows that ABL will significantly increase the turbulence intensity compared with SF. For instance, at height of the flight deck the turbulence intensity is increased from 2% in SF to 10% in ABL. For further information about the features of the flow inside the test section, refer to Zasso et al. [30].

2.5. Scaling parameters

The main scaling objective in this experiment is to correctly replicate the advance ratio of the full scale model, ensuring also the similarity of the reduced frequency. Advance ratio scaling relates three parameters of the test: angular speed of the rotor, geometric scale and free stream velocity. The helicopter model is not a scaled model of an exact aircraft, however could be taken as representative of a medium size helicopter with the geometric scale in the order of 1:13. So, the geometric scale was fixed by the scale of the existing helicopter model. The rotational frequency of the rotor was selected high enough to increase the Reynolds number and Mach number, while reaching the desired advance ratio within the limits of free stream velocity of the wind tunnel test section. Moreover, to avoid issues with vibratory loads caused by high rotational frequency it was decided to limit the angular speed. Consequently, a velocity scale of 1:2.16 was set, leading to frequency scale of 6.08:1 that were both maintained during all tests. The parameters of the scaled helicopter model compared with Bo105, taken as an example of a real medium size helicopter, are summarized in Table 1.

It is worth mentioning that sharp-edged bodies, such as SFS1, are not sensitive to Reynolds number, due to turbulent separation.

Table 1
Parameters of the wind tunnel model and Bo105.

Characteristic	Scaled model	Bo105
Number of Blades	4	4
Rotor Radius (m)	0.375	4.9
Angular Velocity (rad/s)	270	44.4
Blade Chord (m)	0.032	0.27
Free Stream Velocity (m/s)	4.76	10.29
Advance Ratio	0.047	0.047
Tip Mach Number	0.3	0.63
Tip Reynolds Number	2.2e5	3.9e6

In any case, Healy [31] suggests that the ship-based Reynolds number for wind tunnel models should be higher than 11,000 to show this independence. Considering the lower free stream velocity selected for the tests with the helicopter model ($U_\infty = 4.8$ m/s), the Reynolds number of the ship, computed using the ship reference length, is about 350,000 which is well above the minimum required Reynolds number.

3. Experimental results

The experiments were conducted in two different test campaigns. The first campaign was focused on the characterization of the flow field on the flight deck without presence of the helicopter model, while the second campaign was planned to identify the modification to the flowfield, due to the interaction of the helicopter rotor with the ship airwake, and to the loading of the rotor while performing a landing maneuver on the flight deck.

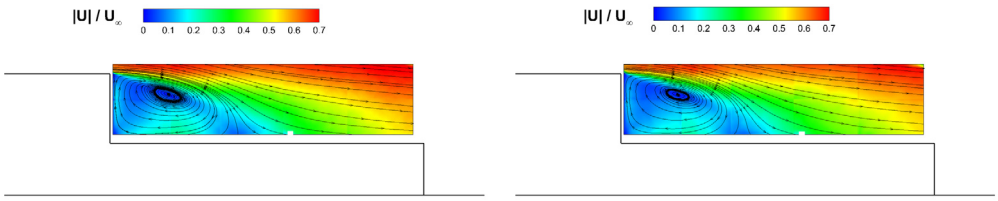

(a) TN1 - $U_\infty = 4.8$ m/s (b) TN3 - $U_\infty = 12$ m/s

Fig. 5. Effect of the free stream velocity magnitude on ship-deck airwake, contours of normalized in-plane velocity magnitude and streamlines in the symmetry plane.

Table 2
Parameters of the first test campaign.

Test number	Advance ratio	Wind direction	No. of PIV planes	Boundary layer type
TN1/TN10	0.0473	H	2/1	SF/ABL
TN2/TN11	0.0828	H	0	SF/ABL
TN3/TN12	0.1182	H	1/1	SF/ABL
TN4/TN13	0.0473	R15	0	SF/ABL
TN5/TN14	0.0828	R15	0	SF/ABL
TN6/TN15	0.1180	R15	0	SF/ABL
TN7/TN16	0.0473	R30	3/1	SF/ABL
TN8/TN17	0.0828	R30	0	SF/ABL
TN9/TN18	0.1180	R30	1/1	SF/ABL

Three wind speeds were selected based on a possible SHOL envelope with a maximum speed of 50 knots at full scale. However, since the rotor cannot be trimmed at high speeds due to the lack of swashplate in the helicopter model, the tests that include the helicopter were performed only at the lowest advance ratio.

A selection of the experimental results of each test campaign is presented separately in the following sections. The complete database is publicly available on request to the authors. It should be mentioned that load measurements in the second campaign will be presented in the rotor reference frame whose x axis is nose to tail, vertical axis is bottom to top and lateral axis points starboard, as represented in Fig. 3(b). The origin of the rotor reference system, representing the reduction point for the measured moments is the center of the rotor.

3.1. Ship airwake investigation

The main objective of this campaign was to assess the topology of the flow field over the flight deck with respect to three parameters: free stream velocity magnitude, wind direction and effect of the presence of the ABL. To do so, nine tests (TN1 to TN9) were conducted with three different wind velocities blowing from three different directions, including head-wind (H) and red wind from 15°(R15) and 30°(R30). The latter two cases refer to the condition in which the wind is blowing from port side of the ship. Pressure measurements were made for all the nine tests with and without presence of the ABL. PIV measurements were performed over three longitudinal planes at different spanwise locations, as shown in Fig. 3(a), and only for few significant cases to limit the testing time. Test parameters of the first campaign are summarized in Table 2, where the advance ratios reproduced in the experiments correspond to 20, 35 and 50 knots for the full scale helicopter.

Fig. 5 compares the PIV measurements of the symmetry plane of the deck for two free stream velocities. In both conditions, the topology of the flow field over the deck is the one commonly seen downstream of a three dimensional backward facing step [32]. The flow field can be decomposed into three main zones: recirculation, reattachment and redeveloping regions as observed in [33]. Regarding the sharp edges of the ship model, the recirculation zone occurs immediately behind the hangar wall and reattaches about half-way along the flight deck. The airwake is directed downward over the recirculation zone, reflecting the fact that streamlines are bending towards the region of low pressure. The comparison between Fig. 5(a) and Fig. 5(b) shows that the structure of the flow field does not change by increasing the Reynolds number, as shown in other studies [34,35]. As a matter of fact, the minimum ship-based Reynolds number of 3.5×10^5 is high enough to create a turbulent flow field and have a flow topology mainly driven by the presence of the sharp edges of the ship. The results shown in Fig. 5 compare well with the investigation performed in [35], where cases with different length of the superstructure and deck are computed. In particular, considering the geometry of SFS1, where the ratio between the length of the superstructure (L_s) and the height of the hangar wall (H_w) is $L_s/H_w = 7.5$, the estimation of the length of the recirculation zone obtained by the experiments is $L_{dr}/H_w = 1.96$, slightly lower that the value estimated using the Improved Detached-Eddy Simulation turbulence model in [35], that is instead equal to $L_{dr}/H_w = 2.0$.

Furthermore, in-plane velocity magnitudes at four sections along the deck, with position X normalized with respect to the length of the deck ($L_d = 2186$ mm), are compared in Fig. 6. It should be mentioned that the height is normalized with respect to the height of the reference Pitot probe, $Z_{\text{ref}} = 1517$ mm. To be more clear, the limits of the hangar wall, from flight deck up to H_w, is specified within a black box. From these diagrams it is possible to estimate the position of the vortex core that is at $X/L_d = 0.82$ and $Z/Z_{\text{ref}} = 0.46$, and that can be compared with the results of Ref. [35] — shown for $L_s/H_w = 7.0$ — equal to $X/L_d = 0.85$ and $Z/Z_{\text{ref}} = 0.47$

Fig. 7 shows the effect of the wind direction on the ship airwake at $U_\infty = 4.8$ m/s. On the symmetry plane, the size of the recirculation zone becomes larger when the wind is blowing from R30, extending the area interested by the vortex in the upper part of the deck. However, the position of the reattachment point is not affected significantly. In this case, almost half of the flight deck is covered by a significantly lower-than-freestream-velocity region which may particularly affect the loading of the rotor and pilot activities during shipboard operations. In the port side plane, the recirculation region starts to develop close to edge of the hangar, while most of the deck remains unaffected, since in this region the air does not flow past the hangar step before arriving to the deck. Moving starboard, the recirculation region increases in size and thus the portion of the shipdeck interested by low-speed flow increases as well. Consequently, it is possible to say that the symmetry of the horseshoe vortex created behind the hangar wall, whose topology is shown in [36,35], is clearly lost when the wind blows from the side, with the vortex core position that seems to drop only on the starboard side. Sectional velocity profiles are compared for this case in Fig. 8 along three PIV planes: starboard, symmetry and port planes. These plots clearly show that starting from the section at $x/L_d = 0.2$, the loss of symmetry between starboard and

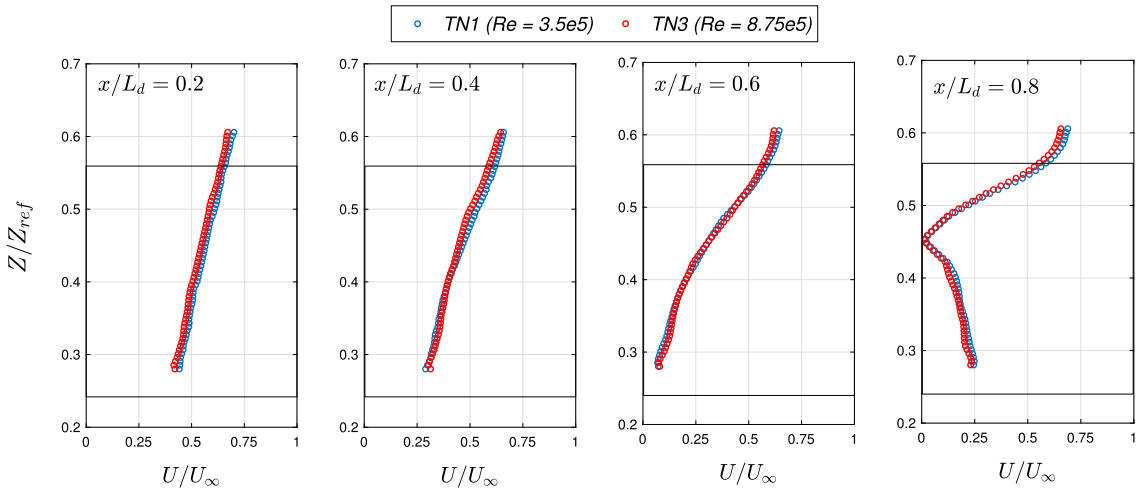

Fig. 6. Time-averaged normalized in-plane velocity magnitude for different stations along the deck on the symmetry plane.

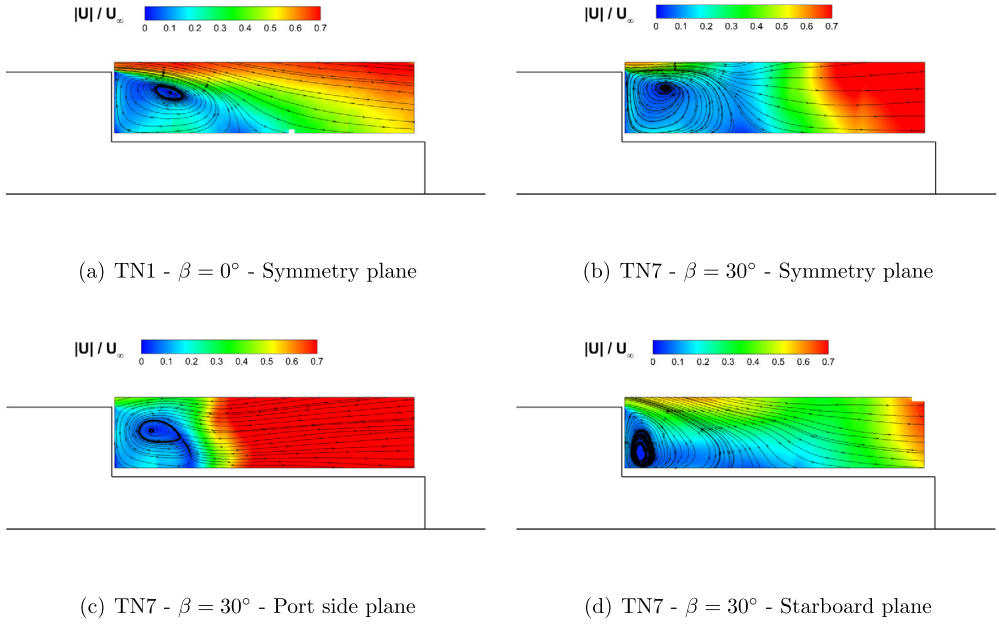

(a) TN1 - $\beta = 0°$ - Symmetry plane

(b) TN7 - $\beta = 30°$ - Symmetry plane

(c) TN7 - $\beta = 30°$ - Port side plane

(d) TN7 - $\beta = 30°$ - Starboard plane

Fig. 7. Effect of the wind direction on shipdeck airwake, contours of normalized in-plane velocity magnitude and streamlines, $U_\infty = 4.8$ m/s.

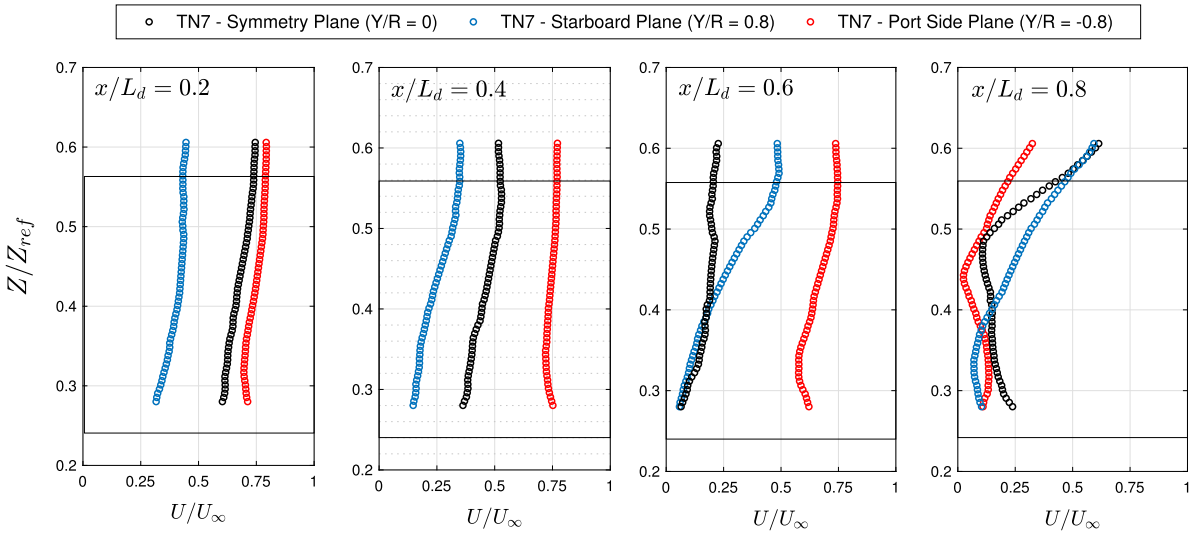

Fig. 8. Time-averaged in-plane velocity magnitude at four sections along three PIV planes.

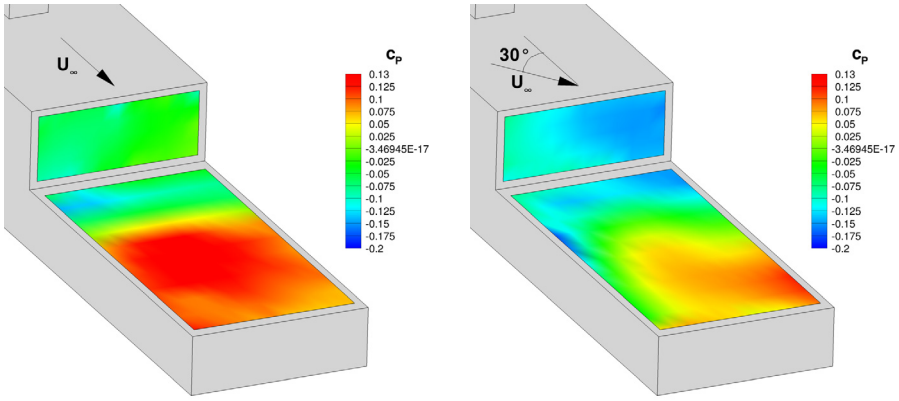

(a) TN1 - $\beta = 0°$ (b) TN7 - $\beta = 30°$

Fig. 9. Effect of the wind direction on pressure coefficient contours of the isolated ship, $U_\infty = 4.8$ m/s.

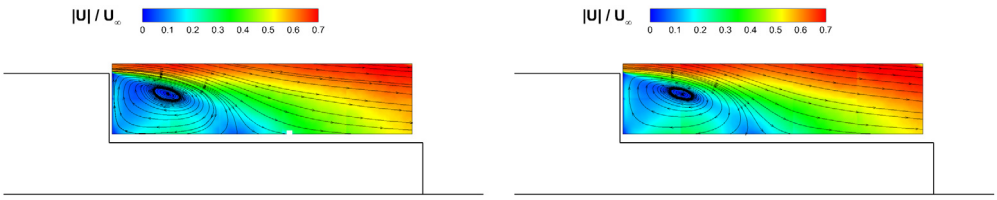

(a) TN1 - $\beta = 0°$ - SF (b) TN10 - $\beta = 0°$ - ABL

Fig. 10. Effect of the ABL on shipdeck airwake, contours of normalized in-plane velocity magnitude and streamlines in the symmetry plane, $U_\infty = 4.8$ m/s.

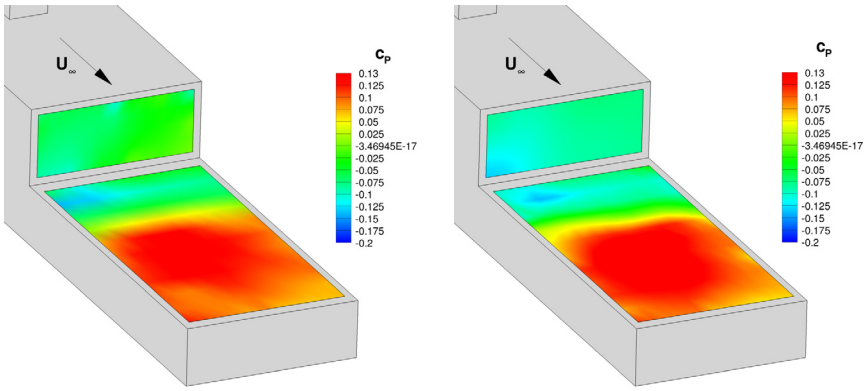

(a) TN1 - SF (b) TN10 - ABL

Fig. 11. Effect of the ABL on pressure coefficient contours of the isolated ship, $U_\infty = 4.8$ m/s, $\beta = 0°$.

port side is quite large. Fig. 8 shows that the rotor blades will experience a significantly different fluid flow while rotating, and that those differences will become steeper while the helicopter will follow a lateral reposition trajectory to enter into the landing region starting from the port side. Those speed differences will be more significant when the aircraft is closer to the hangar wall.

This flow behaviour is confirmed by the comparison of the pressure coefficient distribution measured on the deck for headwind and R30 case, shown in Fig. 9. In particular, looking at Fig. 9(b) for the R30 case, the high pressure recovery region moves downstream and starboard on the flight deck with respect to the headwind case under the influence of the wind blowing from the port side of the ship. A low-pressure region can be observed as well on the starboard side on the hangar wall, differently from the headwind case where the pressure remains homogeneous on this part of the deck.

To quantify the effects of the ABL on the flow field a specific test with turbulators upstream of the ship was performed. Fig. 10 compares the airwake velocity measured on the symmetry plane with SF and ABL in headwind condition. Looking at time-averaged velocities, the airwake structure is very similar. This is further confirmed by the comparison of the pressure coefficient distribution on the deck, shown in Fig. 11. These results are in line with the outcomes of the work by Thedin et al. [37], where the same topology, in terms of time-averaged flow field, resulted from time-accurate CFD simulations of the uniform flow in comparison with steady and unsteady ABL cases. The results presented in [37] demonstrate that the unsteady features due to presence of

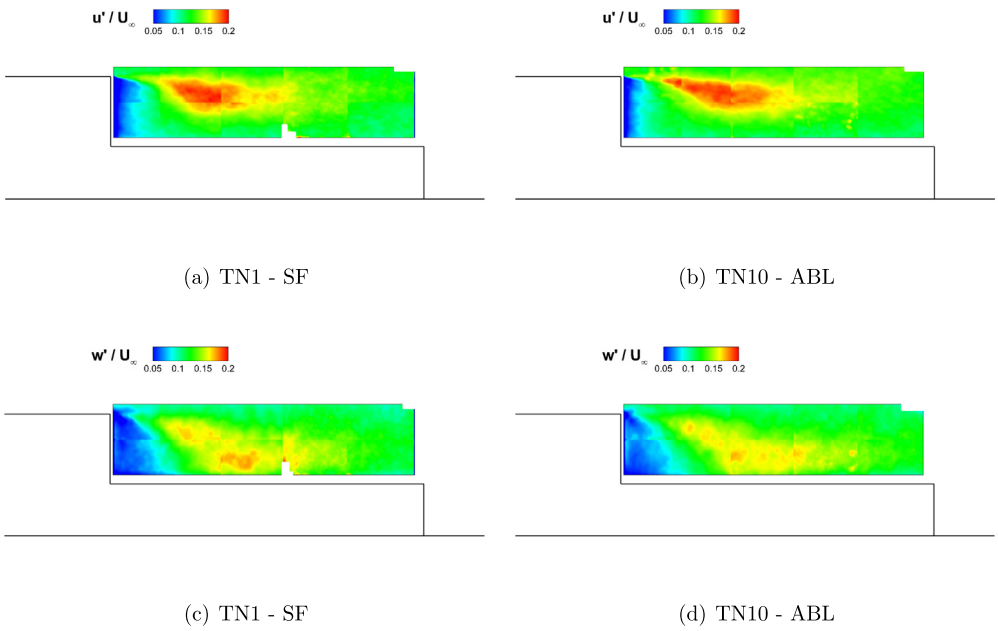

(a) TN1 - SF (b) TN10 - ABL

(c) TN1 - SF (d) TN10 - ABL

Fig. 12. Effect of the ABL on shipdeck airwake, contours of root mean square of the in-plane velocity components, comparison of TN1 and TN10, $U_\infty = 4.8$ m/s.

turbulence in boundary layer are evident only comparing the instantaneous snapshots of the velocity profiles. The effect of ABL was also investigated numerically by Forrest and Owen [38] that compared the results of Detached-Eddy Simulation with flight test data measured at hanger height of Type23 Frigate at Green 10°. The comparisons, made for limited number of data points available from full scale at-sea measurements, showed that CFD computations with ABL and SF predict essentially the same wake pattern. Only, a slightly lower intensity was found for the ABL case in most locations due to the lower incident velocities. However, it should be noted that they did not include the effect of increased free stream turbulence, and ABL model was limited to a logarithmic velocity profile. Moreover, Polsky [39] investigated ABL effect by time-accurate CFD solution of the flow field over the deck of Landing Helicopter Assault (LHA) experiencing beam winds (Red 90°). The outcomes of this work showed that the inclusion of the ABL improved the comparison with experimental data of the averaged flow-field in the plane of one landing point which was completely exposed to the beam wind, while in the areas where the obstruction of the superstructure dominated the flow field the results were not modified significantly.

As a matter of fact, a definite conclusion about the importance of including an ABL in experiments could be provided only by time-resolved PIV measurements showing possible different topologies of the flow field due to the higher unsteadiness level introduced by turbulent ABL profile. However, time-resolved PIV was not available during this test campaign.

The contours of root mean square of the in-plane velocity components evaluated by PIV are presented in Fig. 12 to give an indication of the turbulence level involved in the two cases considered. This comparison also presents a similar behaviour, with comparable values between the SF and the ABL test cases. So, it is possible to assert that in head wind condition, the mean flow over the flight deck is not overly influenced by the presence of the ABL.

Regarding the effect of ABL on rotor trim it should be noted that the flowfield outside the deck is quite different in the two cases. The reason is clear looking at the two velocity profiles in the test chamber for SF and ABL cases shown in Fig. 4. In fact, when the airspeed is the same at the altitude of the Pitot probe, it shows a difference of about 15–20% at the flight deck altitudes. Consequently, it may be expected that the variation of dynamic pressure, between the deck area and outside the deck, will likely affect the flight of helicopter performing the ship landing maneuver.

3.2. Helicopter–ship interaction

The objective of the second test campaign was investigation of the rotor loads during a landing maneuver on the ship deck, affected by the presence of the ship and its airwake. To simulate the landing maneuver, the helicopter was positioned in a series of points representative of a typical stern landing trajectory. The trajectory, as shown in Fig. 13, consists of five points (P1 to P5) that can be divided into two distinctive segments: the initial phase in which the helicopter approaches the flight deck from the stern side along the center line of the flight deck, followed by a descent phase, i.e. an oblique path towards the landing point, which is considered close to the center of the flight deck. Furthermore, three additional points above the landing point were selected to simulate a vertical descent (P5 to P8).

This campaign was conducted first in a condition similar to hover, i.e. with no wind blowing in the wind tunnel, and then for only one free stream velocity ($U_\infty = 4.8$ m/s, corresponding to an advance ratio of 0.0473) blowing from two different directions, i.e. head wind and R30. Indeed, higher free stream velocity could lead to moments beyond the balance full range values due to the impossibility of trimming the rotor. Given the limited differences in mean effect of an ABL on the flow field, helicopter-ship interaction tests were performed without presence of an ABL. Pressure measurements on the flight deck were performed and inflow of the rotor was surveyed by PIV for some selected test points. The position of the rotor center for all test points (P1 to P8) is listed in Table 3, in which the height refers to the vertical offset with respect to the landing spot on the flight deck ($Z - Z_{\text{deck}}$), and X is the distance from the stern of the ship.

Fig. 14 compares the loads measured in hover test for both trajectories with standard IGE models taken from the literature, i.e. Cheeseman & Bennett [40] and Fradenburgh [41]. As shown in [42], they are comparable with the experimental measures at full scale. The same helicopter model used in previous wind tunnel test cam-

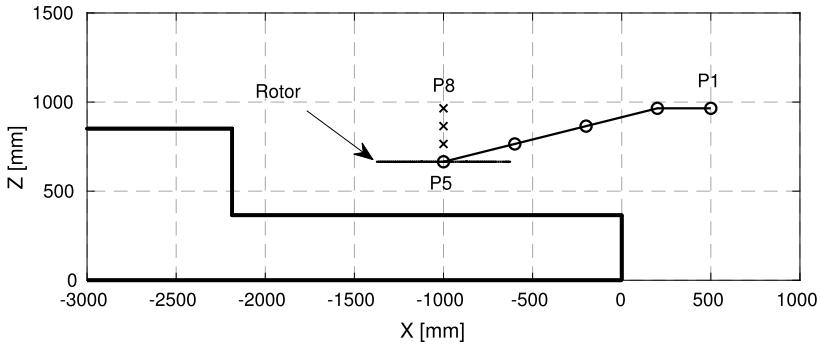

Fig. 13. Side-view of the landing trajectory. Circles and crosses represent the position of the rotor center, respectively in the stern landing and vertical descent.

Table 3
Position of the rotor center along the landing trajectory. The height is measured with respect to the ship deck, except for OGE test which is measured from the ground.

Test point	Height [mm]	Height/R [-]	X [mm]
P1	600	1.60	500
P2	600	1.60	200
P3	500	1.33	−200
P4	400	1.07	−600
P5	300	0.80	−1000
P6	400	1.07	−1000
P7	500	1.33	−1000
P8	600	1.60	−1000
OGE	1135	3.03	700

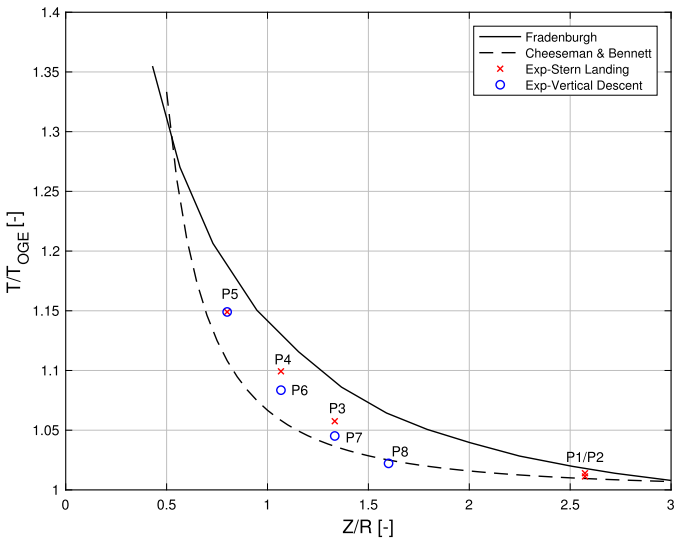

Fig. 14. Ground effect: Comparison of thrust measured during the experiment with data from Cheeseman & Bennett [40] and Fradenburgh [41]. For P1 and P2 the Z/R distance is measured from the wind tunnel ground and not the ship deck.

paign [23] showed a perfect match with Fradenburgh data in ideal IGE conditions. So, all differences shown in Fig. 14 may be associated with the effect of the additional presence of the ship model. It is interesting to see that, at the same altitude from the ship deck, the cases farther from the hangar wall (P3, P4) show always a higher thrust than those closer (P7, P6). An explanation of this difference is given in the following, using moments measurements too. In addition, the partial occlusion of the wake due to the ship deck in P2 is not sufficient to lead to significantly different loads than those obtained in P1.

Fig. 15 compares the thrust and moments measurements in hover and wind-on tests for both landing trajectories. In this figure, the results are expressed in non-dimensional form, normalized with respect to the thrust and torque coefficients measured at OGE position reported in Table 4. As a reminder, the load measurements are cast in the rotor reference frame (i.e. x axis nose to tail, z axis bottom to top and y axis starboard), as represented in Fig. 3(b) implying that a positive pitch moment corresponds to a nose-up moment, and a positive roll moment to port rotation of the rotor thrust.

Table 4
Load coefficients at OGE position.

Rotor position	C_T	C_Q
OGE	7.28×10^{-3}	7.74×10^{-4}

As shown in Fig. 15(a), thrust is increasing as the helicopter approaches the landing point, owing to the ground effect induced by the ship deck. The thrust variation is more significant in hover (wind-off) condition, where an increase of about 15% of the OGE value is obtained at the landing point for the stern landing.

The same behaviour can be observed in vertical landing as well (see Fig. 15(b)). However, the ground effect is less intense with respect to the stern landing at the same height, when considering the wind-off case. For instance, in hover when the helicopter is placed in P6 ($X = -1000$ mm, $Z - Z_{\text{DECK}} = 400$ mm), the rotor experiences only 8% increase in thrust with respect to 10% in P4 ($X = -600$ mm, $Z - Z_{\text{DECK}} = 400$ mm), which is at the same height but farther from the hangar wall. This small difference is caused by the development of a recirculation region between the hangar wall and the helicopter [43], which consists of the fore part of the rotor wake that is deflected by the ship deck and the hangar wall and then re-ingested into the rotor. This causes a slightly increased induced velocity on the fore part of the rotor, together with the consequent thrust loss and a small nose-down (negative) variation of pitch moment particularly apparent for the vertical descent as the helicopter is moved downwards (see Fig. 15(d)). For the stern landing at point P3, the slight peak of the pitching moment can be due to the non-symmetrical ground effect as the rotor disk is only partially inside the flight deck (see Fig. 15(c)). Concerning the roll moment, variations are more limited but a general trend to decrease its value moving toward the flight deck is recognizable for both landing trajectories.

For headwind tests, it can be appreciated that the beneficial effect due to ground is mitigated with respect to hover as can be seen in Figs. 15(a) and 15(b) for both stern landing and the lowermost position of the vertical descent. This is coherent with the vertical induced velocity measured by PIV above the longitudinal symmetry axis of the rotor. Fig. 16 shows the contours of the vertical velocity component measured by PIV at landing point (P5) in hover and headwind condition. In particular, the comparison of the velocity profiles on the lower edge of the PIV measurement

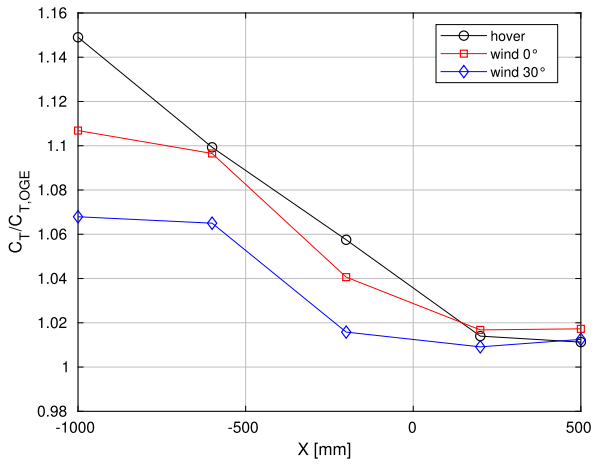

(a) Thrust coefficient, stern landing

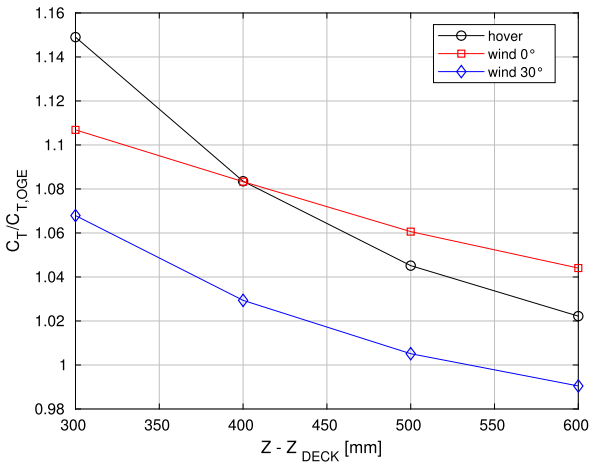

(b) Thrust coefficient, vertical landing

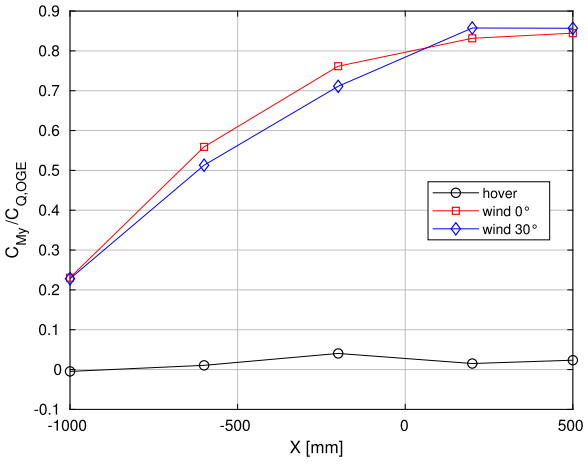

(c) Pitch moment coefficient, stern landing

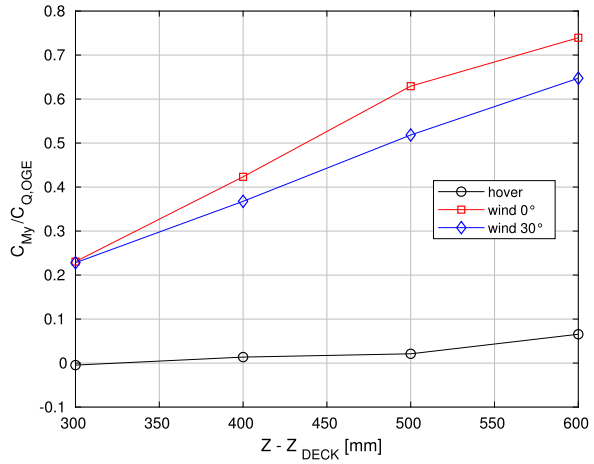

(d) Pitch moment coefficient, vertical landing

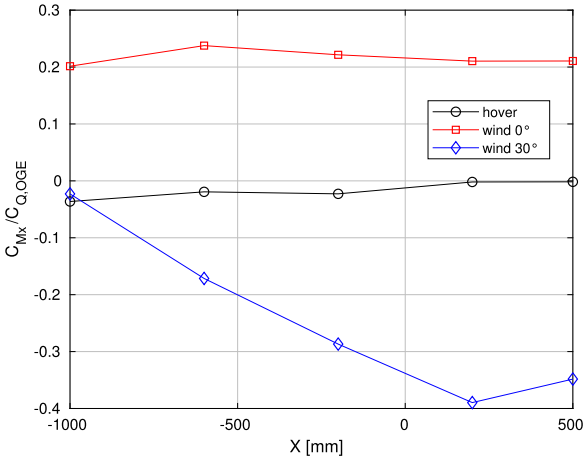

(e) Roll moment coefficient, stern landing

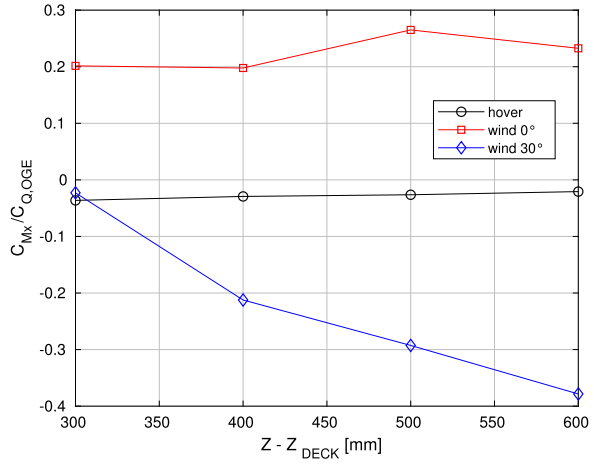

(f) Roll moment coefficient, vertical landing

Fig. 15. Loads acting on the rotor: comparison of stern landing (left) and vertical descent (right), for three different test conditions: hover (TN21), headwind (TN19) and R30 (TN20). On the left, going from right to left, the helicopter is moving from P1 to P5. On the right, going from right to left the helicopter is moving from P8 to P5.

area is shown in Fig. 17(a) as an indication of the downwash on the rotor disk. This figure shows that the reduction of the downwash due to ground effect is clearly mitigated when the wind is blowing.

It should be noted that in the first point (P1) where the helicopter is totally outside of the ship airwake, a large pitch moment is generated by the rotor due to the influence of the external wind on the fixed rotor. As expected, this behaviour is mainly related to

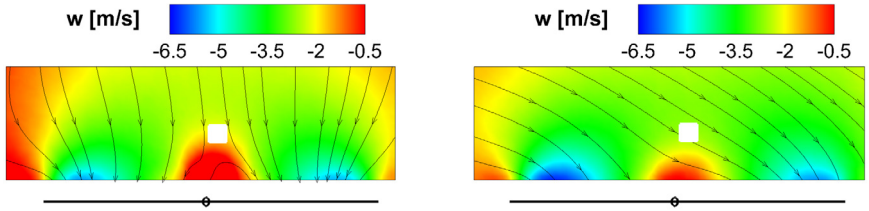

(a) P5 - Hover (b) P5 - Headwind - $\beta = 0°$

Fig. 16. Contours of the vertical velocity component measured by PIV above the longitudinal symmetry axis of the rotor in hover and headwind with rotor positioned at P5.

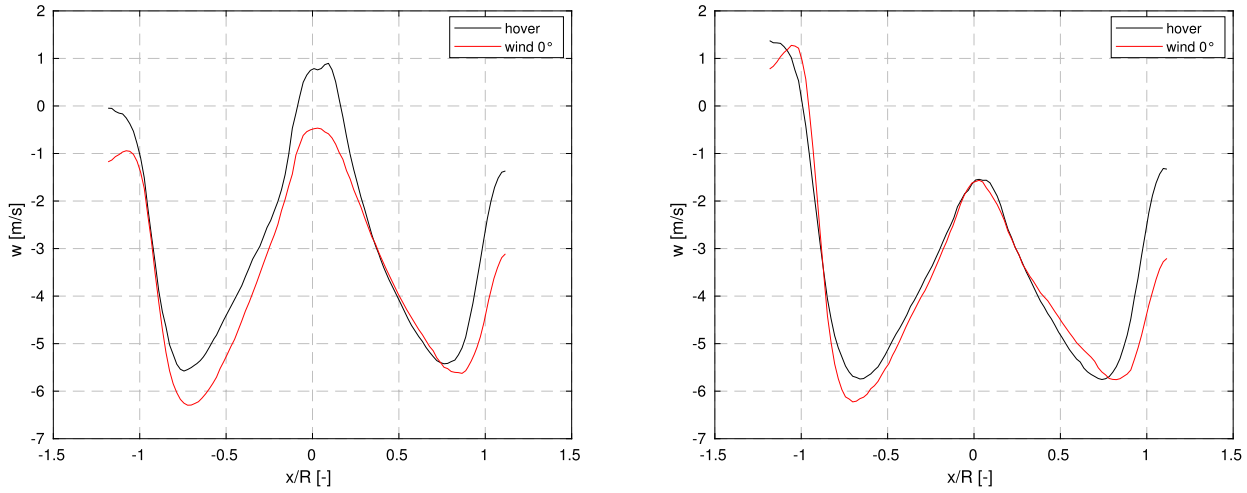

(a) P5 (b) P8

Fig. 17. Profiles of the vertical velocity component measured above the longitudinal symmetry axis of the rotor on the lower edge of the PIV measurement area in hover and headwind with rotor positioned at P5 and P8.

the non-symmetrical induced velocity distribution that is larger in the rear part of the rotor disk as the rotor wake is moving backward. This effect is obviously reduced when the helicopter is in the ship airwake and the horizontal velocity results to be lower, implying significant negative variations of the pitch moment can be appreciated while the helicopter enters the airwake of the ship, about 60% and 45% in stern landing and vertical descent, respectively. Another possible contribution to this is the downwash produced by the recirculation behind the hangar wall on the fore part of the disk that is larger when the helicopter is closer to the flight deck. The comparison of the vertical velocity profiles between P5 and P8 shown in Fig. 17 presents the difference of downwash distribution coherent with the trend of the pitch moment along the vertical descent. On the other hand, the roll moments for both landing trajectories present positive values as expected in headwind condition, while the variations are rather small, although not negligible.

For the R30 tests, the beneficial effect due to ground is more mitigated than in headwind. In particular, about 7% of thrust reduction is observed with respect to hover test when the rotorcraft is placed at landing spot (see Figs. 15(a) and 15(b)). This is even more accentuated during the vertical descent, particularly at P8 in which the thrust reaches a value lower than in OGE condition (see Fig. 15(b)).

Looking at the moment coefficients the most apparent effect with respect to the headwind condition is related to the roll moment, whereas the trend of the pitch moment is quite similar. This could be mainly explained considering the effect of the freestream on induced velocity distribution on the rotor disk as already mentioned for the headwind condition. Indeed, in this case the non-symmetrical distribution from windward to lee side of the rotor disk produces an aerodynamic moment contribution that projected along the longitudinal axis of the helicopter results in a large negative roll moment, as can be seen in Figs. 15(e) and 15(f). This effect is reduced approaching the flight deck due to the reduction of the horizontal velocity, explaining the positive variations of the roll moment measured along both the landing trajectories.

To have a better understanding of the interacting flow field, pressure contours over the flight deck are presented in Fig. 18 comparing the headwind and R30 for three different positions of the helicopter: P5, which corresponds to the landing spot, P4, which is a point on the oblique path and P8, which is the highest point of the vertical path. C_p values higher than one are consistent with the pressure being non-dimensionalised using the wind dynamic pressure, since in the considered test conditions the rotor-induced velocity was higher than the asymptotic wind. Looking at the landing spot (P5), Fig. 18(b), a strong high-pressure region corresponding to the rotor wake impingement area is clearly visible in both cases, but a deeper low-pressure region on the port side of the deck can be appreciated in R30 condition, owing to the wind blowing from the port side of the ship. The pressure contours remain qualitatively similar for the other two test points, however with lower pressure peaks in correspondence to the rotor wake impingement area, related to the higher position of the rotor with respect to the deck. The higher pressure measured in headwind with respect to R30 is coherent with the larger ground effect.

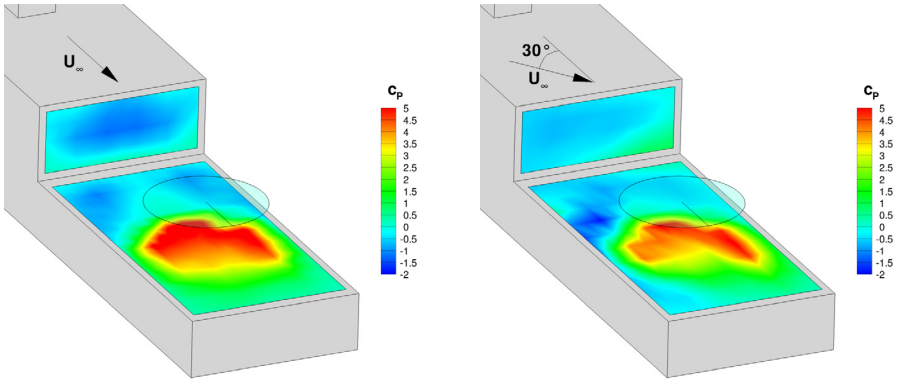

(a) P5, $\beta = 0°$ (b) P5, $\beta = 30°$

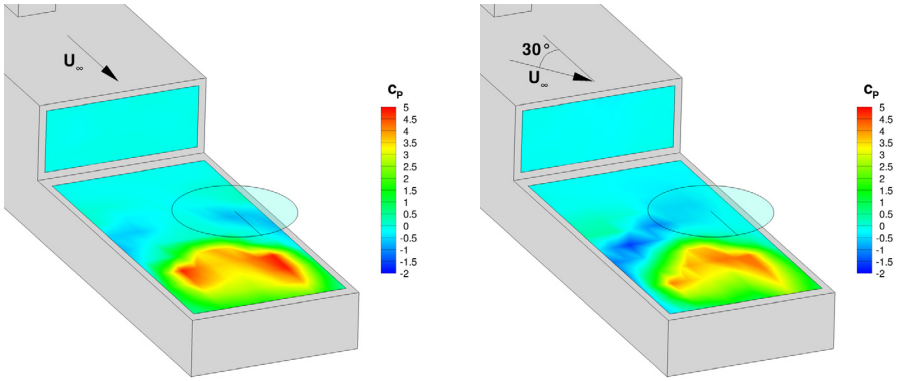

(c) P4, $\beta = 0°$ (d) P4, $\beta = 30°$

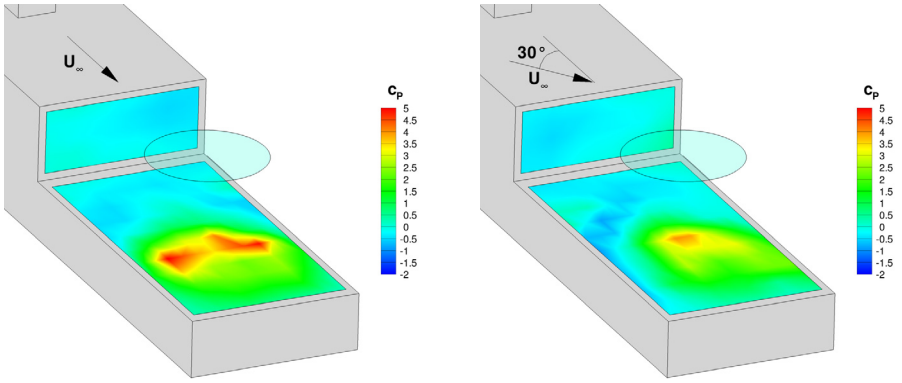

(e) P8, $\beta = 0°$ (f) P8, $\beta = 30°$

Fig. 18. Comparison of the pressure coefficient contours for headwind and R30 with rotor positioned at different height over the deck.

4. Numerical modelling

A multibody model of the experimental rotor has been developed using MBDyn, a free general-purpose multibody dynamics analysis software developed at Politecnico di Milano [44]. MBDyn features the integrated multidisciplinary simulation of multibody systems, including nonlinear mechanics of rigid and flexible bodies subjected to kinematic constraints, along with smart materials, electric and hydraulic networks, active control and essential elements of rotorcraft aerodynamics [45]. The multibody model developed for this study consists of a hingeless, stiff-in-plane rotor with four elastic blades connected to the hub through a revolute hinge, which allows the rotation about the feathering axis of the blade. This degree of freedom, along with a rigid pitch link connected to the swashplate, allows pitch control. The eigenanalysis of the model in vacuum shows that the non-dimensional flapping frequency at nominal rotor speed is $\nu_\beta = 1.22$/rev. The rotor parameters are the same as the scaled model presented in Table 1.

The Blade Element/Momentum Theory aerodynamic model has been considered as well, using a NACA0012 airfoil. The calculation of the loading at the blade tip has been corrected for three dimensional effects considering 2% of aerodynamic tip loss. Moreover, ground effect has been incorporated into the simulation based on the model presented by Fradenburgh in [41].

As mentioned in Section 3.2 the current experiment does not represent a dynamic maneuver, and the load measurements are

only related to the steady response of the rotor. At this stage, the dynamic inflow is not implemented into the simulation environment and the induced velocity field is modelled through a linear velocity distribution over the rotor disk [46]:

$$v_i = v_0(1 + \kappa_x r \cos\psi + \kappa_y r \sin\psi) \tag{2}$$

The classical vortex theory estimates the factors κ_x and κ_y. Drees suggests the following equations to approximate the linear variation of the inflow [46]:

$$\kappa_x = f_x \frac{4}{3}(1 - \cos\chi - 1.8\mu^2)/\sin\chi$$
$$\kappa_y = -2 f_y \mu \tag{3}$$

Here, f_x and f_y are empirical factors used to modify the inflow distribution in both lateral and longitudinal directions ($f_x = f_y = 1$ in Drees model) [47]. These factors have been set in order to generate the same load coefficients, including thrust, torque and in-plane moments, when the helicopter is positioned in the initial point of the landing trajectory (P1). This model has been used as the baseline for the development of the flow distortion identification algorithm explained in the following section.

5. Flow distortion identification algorithm

In order to improve the fidelity of the simulation environment, the flow field of the rotor should be representative of the aerodynamic interaction between the airwake of the ship and the rotor-induced wake. With this aim, an identification algorithm was developed to reconstruct the effect of the variation of the flowfield due to interaction of the rotor wake with the surrounding flow caused by the presence of the ship model. The starting point of this identification were the forces and moments measured on the scaled rotor model. This identified flow distortion is represented through an additional downwash term, that is included as an external input to the simulation environment. This term is expected to reproduce the low-frequency content of the rotor loads response while rotorcraft is moving through the airwake of the ship.

In the present study, the flow distortion velocity is considered to have a linear distribution in radial and azimuthal direction (similar to inflow), defined as the following equation:

$$v_{sh} = v_{sh_0} + v_{sh_c} r\cos(\psi) + v_{sh_s} r\sin(\psi) \tag{4}$$

This simple distribution was chosen because it is the only model who can be identified through the measurement of global rotor thrust and moments. Considering in fact, the relationship between inflow speed and rotor loads described by Peters-He inflow model [48], if the lift distribution on the rotor disk is limited to a linear trend, so that only thrust, pitch and roll moments are the resultants, then only an inflow distribution like Eq. (4) is activated. To identify the coefficients v_{sh_0}, v_{sh_c} and v_{sh_s}, a simple series of optimization problems is solved. First, the average value of the flow distortion v_{sh_0} is identified by looking for the value able to generate the same thrust coefficient measured in the experiment. So, the following minimization objective function (J) has been defined

$$J = \sqrt{(c_T - c_{T_{wt}})^2} \tag{5}$$

where C_T is the computed thrust coefficient with the multibody model and $C_{T_{wt}}$ is the measured one.

Then, the coefficients of the linear distribution of the flow distortion velocity (Eq. (4)), v_{sh_s} and v_{sh_c}, are identified to improve the matching of the in-plane moments. So, in this case the figure of merit for the optimization problem is related to the matching of moment coefficients namely:

$$J = \sqrt{\left(\frac{c_m - c_{m_{wt}}}{c_{m_{wt}}}\right)^2 + \left(\frac{c_l - c_{l_{wt}}}{c_{l_{wt}}}\right)^2} \tag{6}$$

It is notable that the velocity field above the rotor can be considered as the combination of three different terms: the free stream velocity, the inflow of the rotor and the external flow distortion which is representative of the effects produced by the vortical flows generated by the ship. Clearly, inflow and flow distortion velocities at each point above the rotor are functions of load coefficients, advance ratio and position (radial and azimuthal), as indicated in the following equation:

$$\mathbf{U} = \mathbf{U}_\infty + \Delta\mathbf{v} = \mathbf{U}_\infty + \mathbf{v}_{sh}(c_i, r, \psi, \mu) + \mathbf{v}_i(c_i, r, \psi, \mu) \tag{7}$$

where $\mathbf{U}_\infty$ is free stream velocity and $\Delta\mathbf{v}$ is the additional velocity due to the presence of wakes of the obstacle and of the rotor, and c_i are the force and moment coefficients. The simulation results, implementing the solution of the optimization algorithm as an external flow distortion, are compared with the load measurements in headwind condition (TN19) for all test points. In this case the hypothesis of flow distortion perpendicular to the rotor disk has been made, considering the in-plane speed variation negligible with respect to the in-plane velocity generated by the rotor angular speed (Ωr). Fig. 19 compares the rotor loads for both trajectories, including stern landing and vertical descent. The horizontal axis refers to the same coordinate system used in Fig. 15 and all the results are presented in the rotor reference frame, defined in Section 3.

The simulation results are highly consistent with the measurements of thrust and in-plane moments, demonstrating that the external flow distortion field is representative of the effects of the ship airwake on the rotor performance. However, the torque curve computed by MBDyn shows an offset with respect to the experiment. This offset could be related to the additional drag contribution provided by the inner part of the rotor measured in the experiment and not modelled.

The first harmonics of the flow distortion are compared for all test points in Fig. 20. The results show that the initial points of the landing (P1 and P2) do not need additional modification of the velocity field since the effect of the ship airwake on the rotor is negligible. However, moving towards the landing point, the amplitude of the flow distortion is larger, which is consistent with the variation of the in-plane moments (Fig. 19).

The vertical velocity above the longitudinal axis of the rotor is compared with the PIV measurements extrapolated up to the rotor disk, since the closest line of the PIV window was 48 mm above the rotor disk. Fig. 21 shows the results obtained for the cases of the landing point, P5, and point P6 which has a vertical offset with respect to P5. This figure shows with a blue line the distribution of the velocity normal to the rotor disk for the original unmodified model of the rotor. This distribution is clearly uncorrelated with the distribution detected by the PIV. The red line instead, represents the normal velocity distribution obtained by including the flow distortion term, Eq. (4), in the simulation. The slope of the red lines seem in better agreement with PIV distributions that present, in both cases P5 and P6, higher velocity peaks on the left hand side. To further clarify this aspect, Fig. 22 compares the slope of the velocity field distribution calculated joining the two velocity peaks of PIV distributions, with the slopes used in the two multibody models. For both cases, P5 and P6, the inclusion of flow distortion terms allows to recover a positive slope. Furthermore, the magnitude of the slope is higher on P5 than on P6, both for PIV measures and for the models that included the flow distortion terms. Therefore, it is possible to say that the usage of the flow distortion correction terms seems to modify the velocity distribution in a direction that is more compatible with the trends shown by the PIV measures.

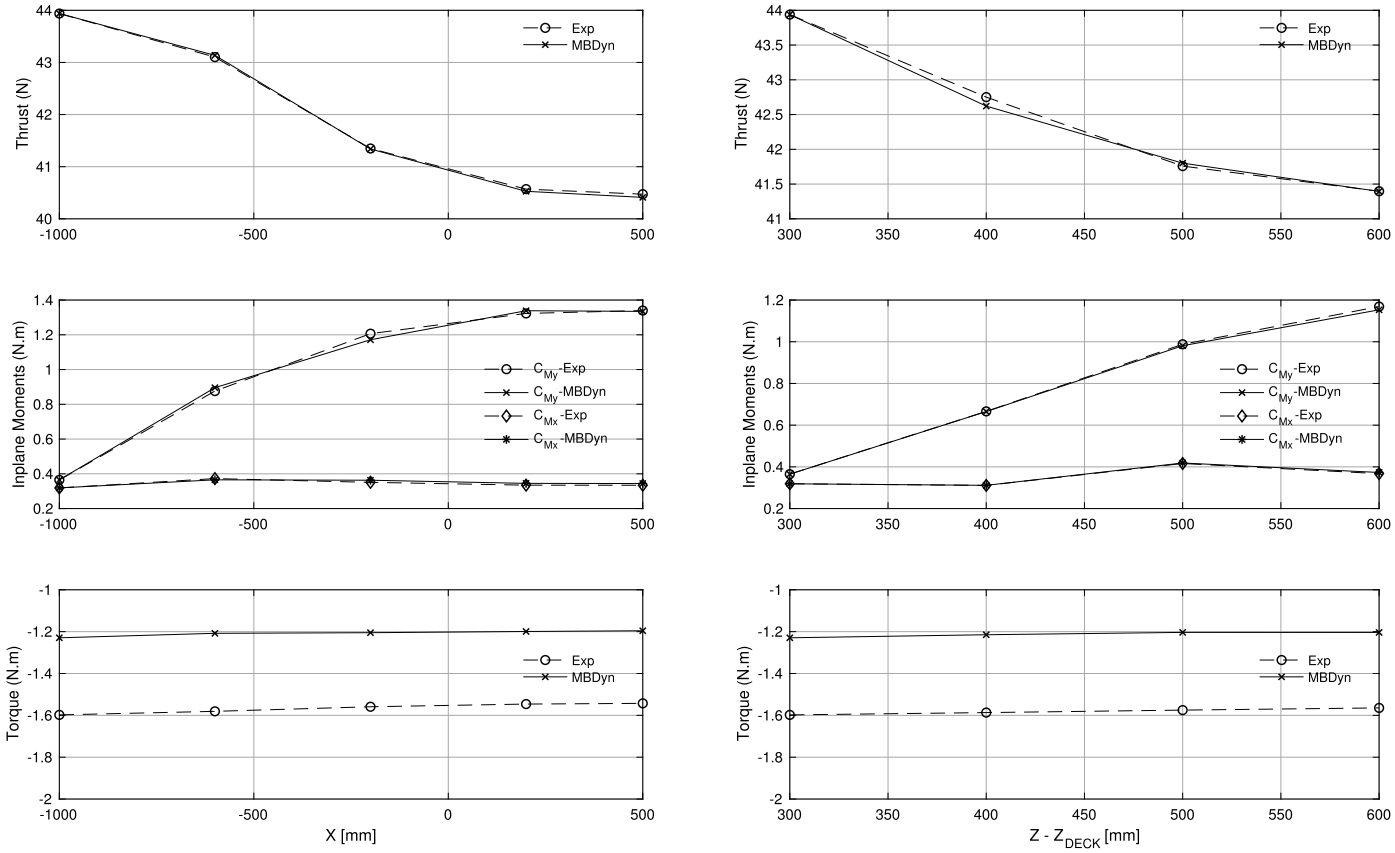

(a) Stern Landing (b) Vertical Descent

Fig. 19. Comparison of rotor loads from experiment and MBDyn simulation, TN19: $U_\infty = 4.8$ m/s, $\beta = 0°$.

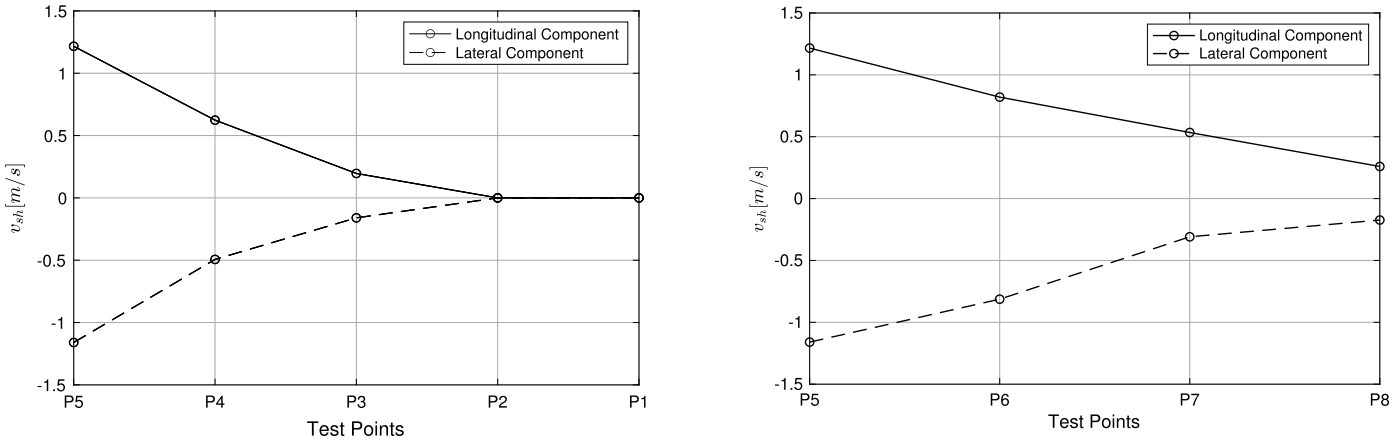

(a) Stern Landing (b) Vertical Descent

Fig. 20. First harmonic of flow distortion in different test points, TN19: $U_\infty = 4.8$ m/s, $\beta = 0°$.

6. Conclusions

This paper presents an experimental study of the aerodynamic interaction between a scaled-down helicopter model and the Simple Frigate Shape 1 model. First, a series of wind tunnel experiments was carried out to study the structure of the flow field over the deck without the presence of the helicopter. This campaign was performed for a range of wind velocity and direction using larger scale models with respect to the literature. Pressure measurements and PIV survey on the flight deck demonstrated the significant effect of wind direction on the size of recirculation zone and its expansion over the flight deck. The atmospheric boundary layer consistent with the coastal area was also simulated in the wind tunnel. The experimental results showed that the presence of boundary layer does not significantly affect the mean flow features over the flight deck, but that can significantly affect the flight dynamics of the aircraft performing the maneuver.

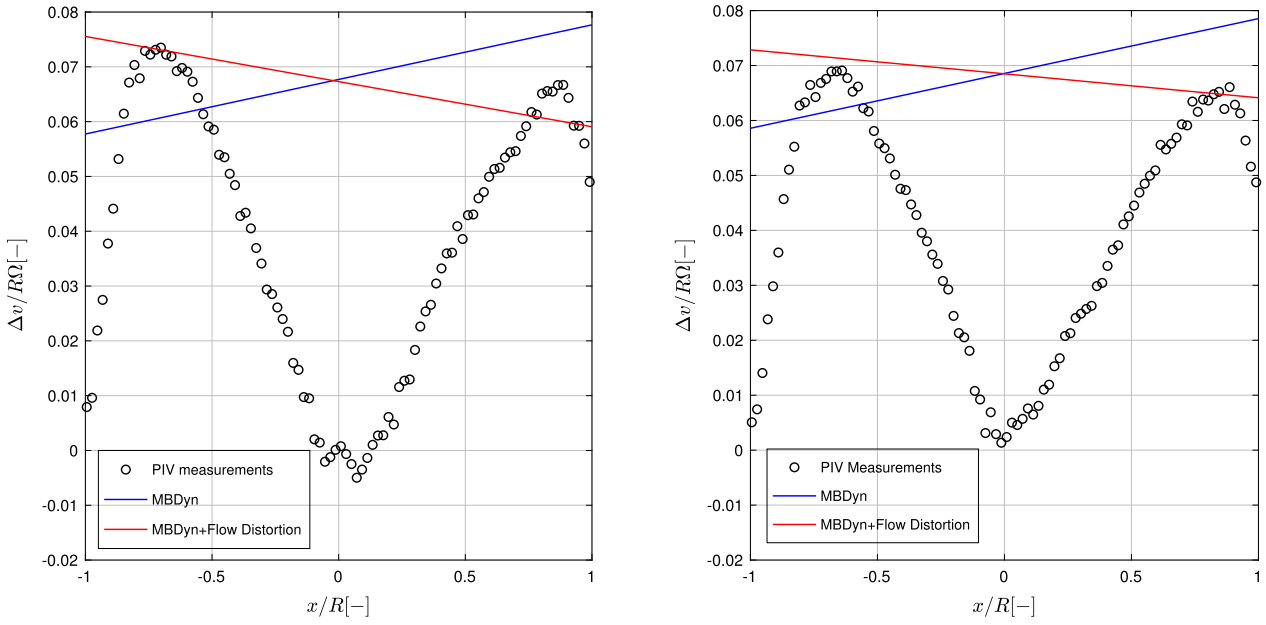

(a) P5 (b) P6

Fig. 21. Normalized vertical velocity along the longitudinal axis of the rotor, comparison of PIV measurement with normal velocity in MBDyn, TN19: $U_\infty = 4.8$ m/s, $\beta = 0°$.

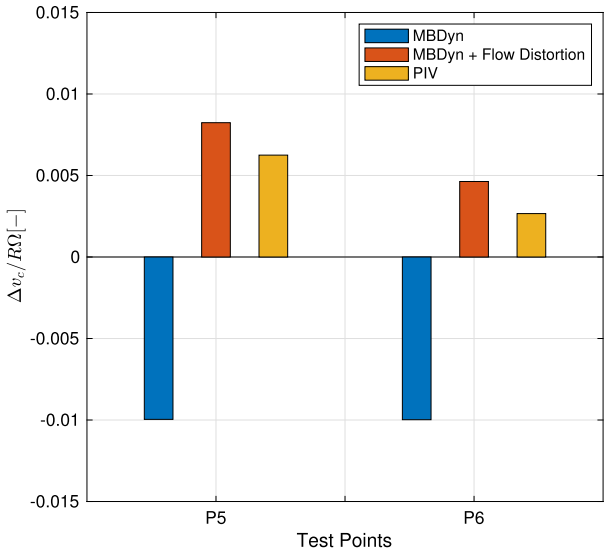

Fig. 22. Comparison of the cosine harmonics of the normal velocity, TN19: $U_\infty = 4.8$ m/s, $\beta = 0°$.

In the second part of the test campaign, the helicopter model was positioned in a series of points representative of a typical stern landing trajectory and a vertical descent above the flight deck, to measure the rotor forces and moments. The ground effect of the deck was noticeable as the thrust increases while helicopter moves towards the deck. This beneficial effect is mitigated in presence of the wind, especially when the wind is blowing from port side of the ship. Regarding the in-plane moments in wind-on tests, there is a significant variation of pitch moment along the landing trajectory which remains almost unchanged in case of headwind and R30. However, the variation of roll moment shows a strong dependency to the wind direction.

The experimental results enabled to achieve a deeper insight about the interactional aerodynamics between ship and helicopter in shipboard operations, particularly useful for the development of high-fidelity simulation environment to improve pilot training. The experimental results were used to develop a preliminary model of the flow distortion effect able to recover a realistic representation of the rotor loads during the simulation of the landing maneuver. However, the identification of unsteady interactional effects will require a modification to the experimental setup to collect the necessary data.

Declaration of competing interest

The authors declare that they have no known competing financial interests or personal relationships that could have appeared to influence the work reported in this paper.

Acknowledgements

This research was supported by NITROS (Network for Innovative Training on ROtorcraft Safety) project which has received funding from the European Union's Horizon 2020 research and innovation program under the Marie Skłodowska-Curie grant agreement No. 721920.

References

[1] S.J. Hodge, S.J. Zan, D.M. Roper, G.D. Padfield, I. Owen, Time-accurate ship airwake and unsteady aerodynamic loads modeling for maritime helicopter simulation, J. Am. Helicopter Soc. 54 (2) (2009) 022005.
[2] D.T. McRuer, Interdisciplinary interactions and dynamic systems integration, Int. J. Control 59 (1) (1994) 3–12, https://doi.org/10.1080/00207179408923067.
[3] L.A. Hoencamp, M.D. Pavel, Helicopter-ship qualification testing for the nh90 nfh helicopter, in: 38th European Rotorcraft Forum, Amsterdam, the Netherlands, 2012.
[4] I. Owen, M.D. White, G.D. Padfield, S.J. Hodge, A virtual engineering approach to the ship-helicopter dynamic interface-a decade of modelling and simulation research at the University of Liverpool, Aeronaut. J. 121 (1198) (2013) 1233–1248, https://doi.org/10.1017/aer.2017.102.
[5] G. Quaranta, G. Barakos, M. White, M. Pavel, M. Mulder, Nitros: an innovative training program to enhance rotorcraft safety, in: American Helicopter Society International 74th Annual Forum, Phoenix, USA, 2018.
[6] D.M. Roper, I. Owen, G.D. Padfield, S.J. Hodge, Integrating cfd and piloted simulation to quantify ship-helicopter operating limits, Aeronaut. J. 110 (1109) (2006) 419–428, https://doi.org/10.1017/S0001924000001329.

[7] C. Crozon, R. Steijl, G.N. Barakos, Numerical study of helicopter rotors in a ship airwake, J. Aircr. 51 (6) (2014) 1813–1832, https://doi.org/10.2514/1.C032535.
[8] G. Chirico, D. Szubert, L. Vigevano, G.N. Barakos, Numerical modelling of the aerodynamic interference between helicopter and ground obstacles, CEAS Aeronaut. J. 8 (4) (2017) 589–611, https://doi.org/10.1007/s13272-017-0259-y.
[9] J. Bludau, J. Rauleder, L. Friedmann, M. Hajek, Real-time simulation of dynamic inflow using rotorcraft flight dynamics coupled with a lattice-Boltzmann based fluid simulation, in: 55th AIAA Aerospace Sciences Meeting, AIAA SciTech Forum, Grapevine, Texas, 2017.
[10] I. Oruc, J.F. Horn, Coupled flight dynamics and computational fluid dynamics simulations of rotorcraft/terrain interactions, J. Aircr. 54 (6) (2017) 2228–2241, https://doi.org/10.2514/1.C034101.
[11] C. Crozon, R. Steijl, G.N. Barakos, Coupled flight dynamics and cfd – demonstration for helicopters in shipborne environment, Aeronaut. J. 122 (1247) (2018) 42–82, https://doi.org/10.1017/aer.2017.112.
[12] J. Zhao, N. Rajmohan, C. He, Physics-based rotorcraft/ship aerodynamic interaction modeling in support of real time flight simulation, in: 51st AIAA Aerospace Sciences Meeting Including the New Horizons Forum and Aerospace Exposition, Grapevine, Texas, 2013.
[13] J.D. Kelle, D.A. Wachspress, J.C. Hoffler, Real time free wake and ship airwake model for rotorcraft flight training applications, in: 71st International Annual Forum American Helicopter Society (AHS), 2015.
[14] I. Oruc, J.F. Horn, J. Shipman, S. Polsky, Towards real-time pilot-in-the-loop cfd simulations of helicopter/ship dynamic interface, Int. J. Model. Simul. Sci. Comput. 8 (4) (2017), https://doi.org/10.1142/S179396231743005X.
[15] S.J. Zan, Experimental determination of rotor thrust in a ship airwake, J. Am. Helicopter Soc. 47 (2) (2002) 100–108, https://doi.org/10.4050/JAHS.47.100.
[16] R.G. Lee, S.J. Zan, Wind tunnel testing of a helicopter fuselage and rotor in a ship airwake, J. Am. Helicopter Soc. 49 (2) (2004) 149–159, https://doi.org/10.4050/1.3092869.
[17] R.G. Lee, S.J. Zan, Wind tunnel testing of a helicopter fuselage and rotor in a ship airwake, J. Am. Helicopter Soc. 50 (4) (2005) 326–337, https://doi.org/10.4050/1.3092869.
[18] C.H. Kääriä, Y. Wang, G.D. Padfield, J.S. Forrest, I. Owen, Aerodynamic loading characteristics of a model-scale helicopter in a ship's airwake, J. Aircr. 49 (5) (2012) 1271–1278, https://doi.org/10.2514/1.C031535.
[19] C.H. Kääriä, Y. Wang, M.D. White, I. Owen, An experimental technique for evaluating the aerodynamic impact of ship superstructures on helicopter operations, Ocean Eng. 61 (2013) 97–108, https://doi.org/10.1016/j.oceaneng.2012.12.052.
[20] Y. Nacakli, D. Landman, Helicopter downwash/frigate airwake interaction flowfield piv surveys in a low speed wind tunnel, in: American Helicopter Society 67th Annual Forum, Virginia Beach, VA, 2011.
[21] D. Stargel, D. Landman, A wind tunnel investigation of ship airwake/rotor downwash coupling using design of experiments methodologies, in: 50th AIAA Aerospace Sciences Meeting, Nashville, Tennessee, 2012.
[22] T. Quinliven, K. Long, Rotor performance in the wake of a large structure, in: American Helicopter Society 65th Annual Forum, Grapewine, TX, 2009.
[23] G. Gibertini, D. Grassi, C. Parolini, D. Zagaglia, A. Zanotti, Experimental investigation on the aerodynamic interaction between a helicopter and ground obstacles, Proc. Inst. Mech. Eng., Part G, J. Aerosp. Eng. 229 (8) (2015) 1395–1406, https://doi.org/10.1177/0954410014550501.
[24] D. Zagaglia, A. Zanotti, G. Gibertini, Analysis of the loads acting on the rotor of a helicopter model close to an obstacle in moderate windy conditions, Aerosp. Sci. Technol. 78 (8) (2018) 580–592, https://doi.org/10.1016/j.ast.2018.05.019.
[25] N. Taymourtash, D. Zagaglia, A. Zanotti, G. Gibertini, G. Quaranta, Wind tunnel investigation of a helicopter model in shipboard operations, in: 45th European Rotorcraft Forum, Warsaw, Poland, 2019.
[26] C. Wilkinson, S.J. Zan, N.E. Gilbert, J.D. Funk, Modelling and simulation of ship air wakes for helicopter operations: a collaborative venture, in: AGARD Symposium on Fluid Dynamics Problems of Vehicles Operating Near or in the Air-Sea Interface, Amsterdam, the Netherlands, 1999.
[27] PIVTEC, PIVview 2C version 3.0, user manual, available online at www.pivtec.com.
[28] A. Zanotti, M. Ermacora, G. Campanardi, G. Gibertini, Stereo particle image velocimetry measurements of perpendicular blade–vortex interaction over an oscillating airfoil, Exp. Fluids 55 (1811) (2014) 1–13, https://doi.org/10.1007/s00348-014-1811-8.
[29] E. Simiu, R.H. Scanlan, Wind Effect on Structures Fundamentals and Applications to Design, 3rd edition, John Wiley and Sons Inc., 1986, p. 46, Ch. 2.
[30] A. Zasso, S. Giappino, S. Muggiasca, L. Rosa, Optimization of the boundary layer characteristics simulated at Politecnico di Milano Boundary Layer Wind Tunnel in a wide scale ratio range, in: Proceedings of the 6th Asia-Pacific Conference on Wind Engineering, Seoul, Korea, 2005.
[31] J.V. Healey, Establishing a database for flight in the wakes of superstructures, J. Aircr. 29 (4) (1992) 559–564, https://doi.org/10.2514/3.46202.
[32] R. Martinuzzi, C. Tropea, The flow around surface-mounted, prismatic obstacles placed in a fully developed channel flow, Trans. Am. Soc. Mech. Eng. J. Fluids Eng. 115 (1993) 85–92, https://doi.org/10.1115/1.2910118.
[33] G.F. Syms, Simulation of simplified-frigate airwakes using a lattice-Boltzmann method, J. Wind Eng. Ind. Aerodyn. 96 (6–7) (2008) 1197–1206, https://doi.org/10.1016/j.jweia.2007.06.040.
[34] S. Zan, Surface flow topology for a simple frigate shape, Can. Aeronaut. Space J. 47 (1) (2001) 33–43.
[35] T. Li, Y. Wang, N. Zhao, Numerical study of the flow over the modified simple frigate shape, Proc. Inst. Mech. Eng., Part G, J. Aerosp. Eng. (2020), https://doi.org/10.1177/0954410020977752.
[36] R. Bardera-Mora, A. Conesa, I. Lozano, Simple frigate shape plasma flow control, Proc. Inst. Mech. Eng., Part G, J. Aerosp. Eng. 230 (14) (2016) 2693–2699, https://doi.org/10.1177/0954410016630333.
[37] R. Thedin, S.M. Murman, J. Horn, S. Schmitz, Effects of atmospheric turbulence unsteadiness on ship airwakes and helicopter dynamics, J. Aircr. 57 (3) (2020), https://doi.org/10.2514/1.C035643.
[38] J.S. Forrest, I. Owen, An investigation of ship airwakes using detached-eddy simulation, Comput. Fluids 39 (4) (2010) 656–673, https://doi.org/10.1016/j.compfluid.2009.11.002.
[39] S. Polsky, Cfd prediction of airwake flowfields for ships experiencing beam winds, in: 21st AIAA Applied Aerodynamics Conference, Orlando, Florida, 2003.
[40] I. Cheeseman, W. Bennett, The effect of ground on a helicopter rotor in forward flight, R & M 3021, ARC, 1955.
[41] E.A. Fradenburgh, The helicopter and the ground effect machine, J. Am. Helicopter Soc. 5 (4) (1960) 24–33, https://doi.org/10.4050/JAHS.5.4.24.
[42] J.G. Leishman, Principle of Helicopter Aerodynamics, Cambridge University Press, Cambridge, MA, 2000.
[43] D. Zagaglia, M. Giuni, R.B. Green, Investigation of the rotor–obstacle aerodynamic interaction in hovering flight, J. Am. Helicopter Soc. 63 (3) (2018) 1–12, https://doi.org/10.4050/JAHS.63.032007.
[44] P. Masarati, M. Morandini, P. Mantegazza, An efficient formulation for general-purpose multibody/multiphysics analysis, ASME J. Comput. Nonlinear Dyn. 9 (4) (2014) 041001, https://doi.org/10.1115/1.4025628.
[45] P. Masarati, D.J. Piatak, G. Quaranta, J.D. Singleton, J. Shen, Soft inplane tiltrotor aeromechanics investigation using two comprehensive multibody solvers, J. Am. Helicopter Soc. 53 (2) (2008) 179–192, https://doi.org/10.4050/JAHS.53.179.
[46] W. Johnson, Rotorcraft Aeromechanics, 1st edition, Cambridge University Press, 2013, p. 136, Ch. 5.
[47] W. Johnson, Development of a comprehensive analysis for rotorcraft. 1 - Rotor model and wake analysis, Vertica 5 (2) (1981) 99–129.
[48] D.A. Peters, D.D. Boyd, C.J. He, Finite-state induced-flow model for rotors in hover and forward flight, J. Am. Helicopter Soc. 34 (4) (1989) 5–17, https://doi.org/10.4050/JAHS.34.5.